ADVANCED ENERGY & SUSTAINABILITY RESEARCH Open Access
www.advenergysustres.com

Mixed Transition Metal Carbonate Hydroxide-Based Nanostructured Electrocatalysts for Alkaline Oxygen Evolution: Status and Perspectives

Ayon Karmakar, Harish S. Chavan, Sang Mun Jeong, and Jung Sang Cho**

Hydrogen is regarded as the cleanest and highest energy-density fuel as an alternative energy resource. Water electrolysis is useful for producing ultrapure hydrogen (>99.9%), and alkaline water electrolysis is industrially adopted for large-scale hydrogen production. However, the anodic oxygen evolution reaction (OER) remains as the bottleneck for achieving efficient hydrogen generation because of its multielectron pathways and sluggish kinetics. Additionally, the OER is crucial for other renewable energy conversion and storage systems, such as CO_2 reduction and metal–air batteries. In this regard, high-performing, durable, and cost-effective electrocatalysts are essential for achieving the desired hydrogen production efficiency. Recently, transition metal carbonate hydroxides (TMCHs) have been investigated as electrocatalysts for alkaline water splitting because of their layered structure, rich redox properties, and high accessibility to electrolytes. Furthermore, the electronic, morphological, and structural modulations in mixed TMCHs, due to the presence of multiple metal centers, offer more accessible active sites for the OER. Considering these aspects, the present review focuses on the application of mixed transition metal carbonate hydroxide (MTMCH)-based nanostructured electrocatalysts to OER in alkaline media. This review will benefit the understanding and evaluation of OER activity and the development of MTMCH-based electrocatalysts for practical application to the OER.

1. Introduction

To date, conventional fossil fuels have been considered the main energy source for modern civilization.[1] The nonrenewable nature and continuous depletion of fossil fuels and the increasing CO_2 emission levels necessitate the development of cost-effective renewable energy conversion/storage systems.[2–5] In this context, hydrogen, as a fuel, is considered an important alternative to many conventional energy resources owing to its several advantages, such as facile energy storage/carrier, high energy density, and zero-emission upon combustion.[6–8] Hydrogen has applications in heat generation,[9] refining processes in industry,[10] and provides electricity in stationary and transport/vehicle.[11] Hydrogen can be manufactured using a variety of methods, such as high-temperature steam reforming, water electrolysis, solar water splitting—thermolysis, and biomass conversion.[12] Among these methods, steam reforming is the preferred method; it fulfills ≈96% of global hydrogen demand.[13,14] However, this process requires high temperatures (700–1100 °C) and fossil fuels/natural hydrocarbons, and it is accompanied by greenhouse gas (CO_2) emissions.[15–17] Among various hydrogen production technologies, water electrolysis can be considered a major contributor to the production of ultrapure hydrogen (>99.9%); moreover, water electrolysis is environmentally benign. In addition, the electrolysis of water in alkaline media is a highly cost-effective, sustainable, and industrially viable method for hydrogen production.[18] However, efficient hydrogen production through water electrolysis is limited by the high overpotential and sluggish kinetics of the anodic oxygen evolution reaction (OER) and the cathodic hydrogen evolution reaction (HER).[11]

The OER involves four-electron transfer pathways under acidic and alkaline conditions. Further, OER is associated with many other energy conversion and storage processes/devices, such as solar fuel production[2] and metal–air batteries.[19] The OER is a four-electron transfer process and has a relatively higher overpotential than the HER and a complex reaction mechanism; hence, OER can be considered the rate-determining step (RDS) for hydrogen production through water electrolysis.[20] Furthermore, the OER has unusually low rate constants and high

A. Karmakar, S. M. Jeong
Department of Chemical Engineering
Chungbuk National University
Cheongju, Chungbuk 28644, Republic of Korea
E-mail: smjeong@cbnu.ac.kr

H. S. Chavan, J. S. Cho
Department of Engineering Chemistry
Chungbuk National University
Chungbuk 361-763, Republic of Korea
E-mail: jscho@cbnu.ac.kr, jscho@chungbuk.ac.kr

The ORCID identification number(s) for the author(s) of this article can be found under https://doi.org/10.1002/aesr.202200071.

DOI: 10.1002/aesr.202200071

overpotentials and induces structural changes in the electrode materials. Consequently, the sluggish kinetics, drop in performance, and ultimately, electrode breakdown account for the poor efficiency of water splitting.[21] Therefore, the overpotential of the OER must be lowered in the presence of suitable electrocatalysts. In this regard, Ru- and Ir- based materials such as Ir/C, Ru/C, IrO_x, and RuO_x are considered commercially available benchmark electrocatalysts.[20] Despite their several key advantages, the large-scale application of these electrocatalysts is limited by their high cost, scarcity, and poor durability in strong alkaline solutions.[17,21–23] In quest of this, a considerable amount of research has focused on developing suitable transition metal (TM)-based electrocatalysts.

Transition metals have received immense attention owing to their high abundance, low cost, high intrinsic activity, and better corrosion stability in alkaline media than Ru- and Ir-based electrocatalysts.[4,24] In addition, there are a number of different methods in the literature to regulate or improve the OER performance of the TM-based nanostructured materials, such as morphological modulations in nanoscale,[25–27] crystal phase and facet engineering,[28,29] heteroatom doping,[30–32] compositional tuning,[33,34] hybrid or heterostructure formation,[35–37] amorphization,[38,39] defect/vacancy creation,[40,41] in situ transformations,[42] ion etching,[43,44] and plasma bombardment.[45–47] In particular, Yin et al. demonstrated that intrinsic oxygen vacancies were highly beneficial to boost the OER performances of NiS_2/CoS_2 nanowires[48] and Ir-single atom decorated $NiCo_2O_4$ nanosheets.[49] In contrast, high electrocatalytic activity with improved structural stability and conductivity was realized in Co-doped NiS_2 nanosheets[50] and Cl-doped $LaCoO_3$ hollow cubes.[51] Therefore, TM-based electrocatalysts, such as oxides, hydroxides, carbonate hydroxides, borides, sulfides, selenides, phosphides, carbides, and nitrides, can be considered as potential alternatives to precious electrocatalysts for the OER in alkaline media.[52,53] Among the TM-based electrocatalysts, oxides, hydroxides, and carbonate hydroxides are preferable for electrochemical water splitting owing to their low cost, easy synthesizability, environmental friendliness, moderate conductivity, and most importantly, stability in alkaline media.[52]

Transition metal carbonate hydroxides (TMCHs) have recently received considerable attention as efficient OER electrocatalysts. TMCHs offer various advantages—low cost; layered structures that facilitate mass transfer at the electrode–electrolyte interfaces; improved hydrophilicity due to the interlayer CO_2^{3-} ions, which enhances the wettability and OH^- adsorption at the electrocatalyst surface in alkaline media; high surface area with an increased active-site accessibility; and long-term stability.[54–58] Despite these advantages, TMCHs suffer from low electronic conductivity, which leads to slow reaction kinetics and large overpotentials.[59] For instance, Wang et al.[59] reported carbon cloth (CC)-supported cobalt carbonate hydroxide hydrate (CCHH) nanowires exhibiting an overpotential (η_{10}) of ≈323 mV in the alkaline OER (1.0 M KOH). In another study, CCHH nanosheets required an overpotential of ≈315 mV to deliver 10 mA cm^{-2} current density in the OER.[60] Although these indicate moderate OER activity, more reduction of overpotential and improvement in kinetics are desirable to achieve efficient water electrolysis. In addition, the high hydrogen and water adsorption free energies (ΔG^*_{H} and $\Delta G^*_{H_2O}$) are responsible for the poor water-reduction ability of TMCHs.[61] The limited number of available active sites and intrinsic activity of monometallic TMCHs can be addressed by considering multimetallic analogs. In this context, mixed transition metal carbonate hydroxides (MTMCHs) exhibit enhanced performance in electrocatalytic water splitting under alkaline conditions owing to the synergistic effect between multiple metal species, variable oxidation states of the cations, the possibility of reversible surface redox reactions, presence of enhanced active centers, and optimized MTM chemical compositions.[6,20,62–64] Furthermore, owing to the low activation energy for the electron transfer between metal cations in an MTM, the electronic conductivity of MTM-based materials may be higher than that of their monometallic counterparts.[63,65,66]

In view of the aforementioned discussions, this review presents a brief survey of the literature on the electrocatalytic activity of MTMCHs in the OER. **Figure 1** displays a pie chart of the available reports on the electrocatalytic alkaline OER activities of transition metal carbonate hydroxides to date.[55–57,59,60,67–99] The present review commences with a general discussion of the electrochemical pathways and mechanism of OER in alkaline media. Subsequently, all the activity-determining parameters in the OER and comprehensive studies on first-row transition-metal-based multimetallic MTMCHs as OER electrocatalysts are discussed. The various design strategies, such as compositional tuning, heteroatom doping/substitution, morphology modulations, in situ transformations, and hybrid/composites, for enhancing the OER performance are then explored. In conclusion, the current status, challenges, and future perspectives of using MTMCHs as OER electrocatalysts are summarized.

2. Mechanism of OER

The OER/ water oxidation is a preliminary step in photosynthesis as well as in renewable energy conversion and storage technologies, such as water electrolyzers, metal–air batteries, and solar fuel production.[23] This anodic oxidative reaction provides the required protons and electrons for the cathodic half-cell reactions (reduction), such as H_2 generation, CO_2 reduction, and N_2 reduction.[6] In general, the OER in alkaline media undergoes a necessary elementary step involving the coordination of

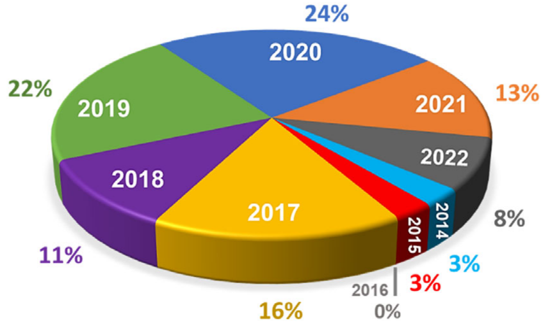

Figure 1. Pie chart of literature on alkaline oxygen evolution reaction (OER) performance of transition metal carbonate hydroxides (TMCHs).

OH^- to the surface of the active sites of the electrocatalysts. The alkaline OER at the anode can be expressed as follows[100]

$$4OH^-(aq) \rightarrow 2H_2O(l) + 4e^- + O_2(g) \uparrow \tag{1}$$

The active metal centers (M) on the surface of the electrocatalyst usually participate in the OER. The commonly accepted mechanism of alkaline OER, as proposed by several researchers, is described in Equation (2)–(6) and depicted in **Figure 2**a.

$$M + OH^- \rightarrow M - OH + e^- \tag{2}$$

$$M - OH + OH^- \rightarrow M - O + H_2O + e^- \tag{3}$$

$$M - O + M - O \rightarrow 2M + O_2 \tag{4}$$

$$M - O + OH^- \rightarrow M - OOH + e^- \tag{5}$$

$$M - OOH + OH^- \rightarrow M + O_2 + H_2O + e^- \tag{6}$$

According to the abovementioned mechanism, the initially adsorbed OH^- ions on the electrocatalyst surface undergo oxidation by releasing one electron to form $M - OH$. Subsequently, $M - OH$ reacts with another OH^- to produce $M - O$, followed by the release of another electron. Thereafter, $M - O$ can follow two different pathways to form molecular O_2. The intermediate $M - O$ either recombines with another $M - O$ to release O_2 gas or forms $M - OOH$ upon reacting with OH^-, followed by decomposition into O_2.[52,101–103] However, the $M - O$ bonding interactions in $M - OH$, $M - O$, and $M - OOH$ intermediates are a few key parameters in electrocatalytic OER performance.[52] Furthermore, it is difficult to precisely determine the reaction kinetics and RDS of the OER owing to the multiple electron transfer pathways and intermediates.[104] Hence, DFT calculations have been performed to understand the reaction mechanism of each step and to provide a thermodynamic model of the electrochemical reactions.[105–107] Here, the change in the adsorption energy of the two intermediates determines the reaction energy of the individual elementary reaction step. The least thermodynamically favorable step can be identified from the reaction free energy diagrams (Figure 2b), as suggested by Dau et al.[108] Irregular changes in the adsorption energies of the intermediates led to a different reaction energy in each step. As a result, the reaction step with the highest free energy was considered the RDS.[108] Furthermore, Valdes et al.[109] observed that the M–OOH formation was rendered difficult by strong oxygen binding to the electrocatalyst surface; in contrast, weak oxygen binding rendered the M–O formation difficult. Moreover, the binding energies of the intermediates depend on several factors such as the adsorbed species, solvent interactions, and surface vacancies.[20] In view of this, the role of oxygen (O) and hydroxyl (OH) surface coverage in the OER performance of rutile oxides, such as RuO_2, IrO_2, and TiO_2, was investigated by Nørskov et al.[106] In the case of RuO_2, M–OOH formation energy was highest with O-surface coverage, whereas M–O intermediates were hardly stable with HO-surface coverage; thus, the surface conditions of the electrocatalyst influence the intermediate formation. Additionally, the M–OH and M–OOH intermediates were more stable than the M–O intermediate owing to the hydrogen bonding between the –OH groups.[106] In addition, the interactions of the water molecules with the electrocatalyst surface also influence the OER ability.[110] Because electrocatalytic oxygen evolution is highly susceptible to multiple parameters, a unique microscopic parameter that can serve as an RDS descriptor is essential. In this regard, various descriptors, such as the M–OH bonding energy, energy of the reaction step ($\Delta G_{O*} - \Delta G_{HO*}$), and certain electronic structural parameters (d orbital occupation, e.g., orbital filling, and O *p*-band center), have already been reported to demonstrate the OER mechanism.[20] In summary, OER electrocatalysts can be further developed from a thermodynamic perspective to decrease the activation energy barrier for oxygen evolution.

3. Parameters Used to Evaluate Electrocatalytic Activity

The suitability of any electrocatalyst for the OER is assessed by performing electrochemical measurements involving various parameters. The significance of those key parameters in investigating the electrocatalyst performance in water splitting is discussed briefly herein. Current density (j) is the current normalized with respect to the geometrical/electrochemically active surface area of the working electrode. In practice, electrochemical water oxidation occurs at a potential much higher than the thermodynamic potential ($E^0 = 1.23V$). This excess potential is referred to as the overpotential (η)[100] and is ascribed to the high activation energy, sluggish charge transfer kinetics, poor

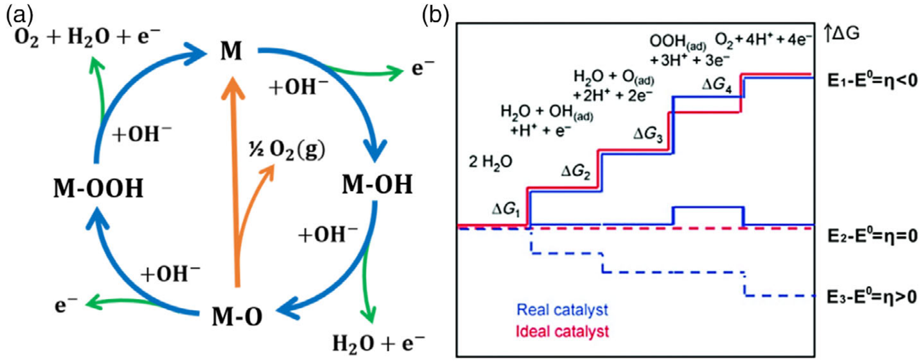

Figure 2. a) Schematic of the electrocatalytic OER mechanism on an electrode surface in alkaline media. b) Gibbs free energy diagram for alkaline OER involving different oxygen intermediates. Reproduced with permission.[108] Copyright 2010, Wiley-VCH GmbH.

electrode conductivity, ionic/gas diffusion limitations, and poor energy efficiency.[6,62,111] In general, the value of the overpotential (η) is calculated at a given current density (10 mA cm^{-2}) from the iR-compensated current–potential curve (LSV curve). The overpotential (η_{OER}) for real-time water oxidation, considering the ohmic potential loss (iR), can be expressed as follows

$$\eta_{\mathrm{OER}} = E - 1.23 - iR \tag{7}$$

where E, i, and R are the measured potential (V) at a current density, current (A), and solution resistance (Ω) determined by electrochemical impedance spectroscopy (EIS), respectively. The Tafel slope (b) is another key parameter for studying the reaction kinetics, mechanism, and intrinsic activity of an electrocatalyst.[112] It is related to the overpotential (η), current density (j), and exchange current density (j_0), as shown below[6]

$$\eta = b \log\left(\frac{j}{j_0}\right) \tag{8}$$

The Tafel plot is derived from the iR-compensated polarization curve, and the linear portion of the curve provides the value of the Tafel slope. Further, a linear extrapolation of this plot up to $\eta = 0$ provides j_0 value of the electrocatalyst. The j_0 value obtained herein is related to the physical, structural, and other factors that influence the surface properties of the electrode–electrolyte interface.[113] The intrinsic activity of an electrocatalyst is expressed in terms of the turnover frequency (TOF), which is defined as the number of molecules produced per active site per unit of time from the number of reactants. Generally, the TOF of heterogeneous electrocatalysts is calculated by considering the active sites present on the electrocatalyst surface. The TOF can be calculated using the following equation[114]

$$\mathrm{TOF} = \frac{jN_A}{nF\Gamma} \tag{9}$$

where j, N_A, n, F, and Γ are the current density at an overpotential, Avogadro's constant, number of electrons transferred, Faraday constant, and number of moles of active sites present in the electrocatalyst, respectively. The concentration of the active sites can be determined using different techniques such as cyclic voltammetry (CV) and inductively coupled plasma spectrometry by assuming that all the metal centers present in the electrocatalyst are electrocatalytically active. However, precise identification of real active sites for OER is challenging; it could be achieved using in situ spectroscopic techniques such as Raman spectroscopy, X-Ray photoelectron spectroscopy (XPS), and X-Ray absorption spectroscopy (XAS).[114,115] In this context, in situ Raman spectroscopy is useful to identify the intermediates and structural transformations of the electrocatalysts during electrocatalytic OER by monitoring the changes in low-frequency vibrational modes.[114–117] For example, Qiu et al.[118] observed that the formation of γ-NiOOH was responsible for the improved OER activity of NiFe-LDHs in alkaline media. The presence of Fe^{3+} influenced the oxidation of Ni^{2+} into γ-NiOOH, which was identified as the OER active phase by in situ Raman spectroscopy.[118] In another report, in situ Raman spectroscopy indicated successive oxidation of $\mathrm{Co_3O_4}$ to CoOOH with increasing oxidative potential during OER in gold-supported $\mathrm{Co_3O_4}$.[101] Further, Co^{4+} species were identified as the real active sites for OER. The changes in the elemental bonding environments, present in the electrocatalyst, during the course of OER can be monitored by in situ XPS. Ali-Löytty et al.[119] utilized XPS at ambient pressure to probe the changes in the surface chemical structure of the electrodeposited NiFeOOH thin film during OER. The oxidation of Ni and Fe was identified from the in situ Ni and Fe 2p XPS spectra under the anodic potential of OER.[119] In situ XAS in combination with the Extended X-Ray absorption fine structure (EXAFS) and X-Ray absorption near edge structure (XANES) can be utilized to detect the modifications of the electronic structure as well as the local geometric environments of the atoms of the electrocatalysts.[114] Bell and coworkers observed the octahedral occupancy of Fe^{3+} ions in $\mathrm{Ni_{1-x}Fe_xOOH}$ and very short Fe–O bond distances by operando XAS technique during alkaline OER.[120] The authors also indicated that the amount of Fe (<25%) was critical in achieving Fe-doped γ-$\mathrm{Ni_{1-x}Fe_xOOH}$ to exhibit high OER activity. Adding to this, DFT studies suggested Fe^{3+} as the true active sites for OER in such Ni-Fe-based materials.

The accelerated and long-term stabilities of electrocatalysts can be successfully studied by chronopotentiometry/chronoamperometry and CV. Accelerated stability is measured by subjecting the electrocatalysts to CV cycles ($\geq$1000) at high scan rates ($\geq$100 mV s^{-1}). Long-term stability is studied by chronopotentiometry (at a constant current density, typically 10 mA cm^{-2})/chronoamperometry (at a constant potential) for $\geq$12 h. In general, the corresponding negligible increase in the overpotential at 10 mA cm^{-2} or decrease in the current density demonstrates the stability/durability of an efficient electrocatalyst. However, the electrocatalyst stability deteriorates with the exfoliation of the electrode material due to the intense gas evolution and corrosive nature of the high pH electrolytes.

4. General Synthetic Methods for Preparation of MTMCH Electrocatalysts

There are various methods—hydro-/solvo-thermal, coprecipitation, reflux, electrodeposition, and atomic layer deposition—for fabricating oxides, metal carbonate hydroxides, and their hybrids or nanocomposites.[62,121–124] In this section, different preparatory techniques adopted for MTMCHs will be briefly highlighted.

4.1. Hydrothermal or Solvothermal

Inorganic nanostructured materials with various morphologies and compositions can be fabricated using hydrothermal or solvothermal methods in the presence of aqueous or nonaqueous solvents, respectively. In this process, a solution of reactants is reacted at elevated temperature and pressure inside a sealed autoclave. The morphology, size, composition, and structure of the products can be tuned by altering the reaction parameters, such as the solvent, temperature, time, reactant concentration, and pH. The safety issues due to autogenerated high pressure at elevated temperature, requirement of expensive autoclaves, and unavailability to observe the changes during the reaction are a few disadvantages of this method.[125] Despite these issues, the hydrothermal/solvothermal process is also advantageous for the direct growth of nanoarchitectures on the 3D conducting substrates.[126] These direct-grown self-supported materials are useful as binder-free electrode materials for OER. In addition, firm contact between nanostructured materials and 3D substrates makes the electrocatalysts more robust for long term applications in OER. In view of these advantages, a wide range of MTMCH-based electrocatalysts and most of the directly grown materials on Ni-foam (NF), Cu-foam (CF), and carbon cloth (CC)/carbon paper (CP), and graphite paper (GP) are fabricated by this technique. For example, Yang et al.[74] employed a two-step hydrothermal approach for preparing partially sulfurated NiFe carbonate hydroxide (Ni_xFe_yS/CH) nanosheets. Initially, Ni_xFe_yCH was hydrothermally synthesized with different Ni/Fe molar ratios at 120 °C, and the second hydrothermal step was used for the controlled sulfurization of the previous Ni_xFe_yCH by changing the sodium sulfide concentration at 160 °C for 8 h. Tang et al.[75] grew a series of Co_xMn_yCH samples directly on Ni foam with varying Co/Mn ratios (from 2:0 to 0:2) through a one-step solvothermal technique, using a mixed solvent (ethylene glycol/ethanol). In another study, Ni and Mn substitution in cobalt carbonate hydroxide (CCH) along with direct growth on GP were achieved via a simple one-step hydrothermal reaction at 160 °C for 24 h.[76] The formation mechanism suggested that urea was the source of NH_3 and CO_2 in the reaction mixture, which reacted with the metal ions under the experimental conditions and were further converted to OH^- and CO_3^{2-} ions, respectively. NiCo carbonate hydroxide nanowires on Ni foam were fabricated by employing a polyvinyl pyrrolidone (PVP)-assisted hydrothermal technique at 180 °C for 12 h in a 50 mL autoclave.[84] The role of urea hydrolysis in providing OH^- and CO_3^{2-} ions for the crystal growth was determined; however, the role of PVP was unclear. Furthermore, these NiCo carbonate hydroxide nanowires were treated with Ar plasma for different durations ranging 5–30 min. Kang et al.[88] adopted a low-temperature hydrothermal method to fabricate a Cu-foam-supported $Cu(OH)_2$@CoNi carbonate hydroxide core/shell hybrid. They used room-temperature grown $Cu(OH)_2$ nanotubes on Cu foam as the substrate/core to hydrothermally grow CoNiCH nanothorns on the walls of the $Cu(OH)_2$ nanotubes at 85 °C for 3 h in a 50 mL autoclave. In another study, a two-step hydro-/solvo-thermal process was implemented to prepare a NiFe-MOF/Fe carbonate hydroxide heterostructure on Ni foam.[99] The synthesis procedure comprised the initial hydrothermal preparation of FeCH on Ni foam and the subsequent solvothermal reaction in a mixed solvent (DMF/ethanol/H_2O) using FeCH/NF as the template and terephthalic acid to obtain the NiFe-MOF/FeCH-NF hybrid.

4.2. Coprecipitation

Coprecipitation is another facile and inexpensive wet-chemical method for preparing electrocatalysts. In this method, the desired material is prepared by mixing metal salt solutions with stirring, followed by precipitation resulting from the pH change of the medium. The need for surface protecting agents, such as surfactants, ligands, and chelating agents for controlling the size/shape of the nanostructured materials is the main disadvantage of this technique.[100] However, the main advantage of coprecipitation is low or room temperature processing and is also useful for producing amorphous structures, which are considered beneficial for the electrocatalytic OER.[127] For example, Karthick et al.[72] synthesized nickel–iron hydroxy carbonate hydrate (NiFeHCH) nanosheets by coprecipitation at room temperature within 1 h. In this process, upon adding a desired stoichiometric ratio of aqueous Ni- and Fe-salt solutions to a 0.5 M Na_2Co_3 aqueous solution, a light green precipitate appeared immediately, indicating the formation of NiFeHCH. The color changed to dark green upon further stirring for up to 1 h. Their group also reported a similar strategy for fabricating nickel–cobalt carbonate hydroxide hydrate (NiCoCHH) cubic nanostructures,[73] wherein metal acetate salts were used as Ni and Co precursors with the Ni/Co molar ratios ranging from 0.5 to 1.5. The rest of the preparation procedure was the same as that described previously.

4.3. Electrodeposition

Electrodeposition is another widely used method for preparing thin films of electrocatalysts on desired conducting substrates. To date, several thin films of hydroxides, oxides, phosphates, carbonates, nitrides, phosphides, and chalcogenides have been successfully deposited on the electrode surface by reducing/oxidizing the metal ions present in the electrolytes.[100,128,129] Further, the main advantage of this method involves control over the quality and thickness of the nanostructured films by changing the applied potential or current and deposition times at the electrodes.[100,130] Although, lack of control in fabricating different nanostructured morphologies and unsuitability of large-scale production are the disadvantages of this technique.[131] Reports on MTMCHs infer that electrodeposition has mostly been used for modifying the surface of presynthesized metal carbonate hydroxides.[93,97,98] For example, Cai et al.[93] electrodeposited a CeO_2 layer on hydrothermally prepared carbon fiber paper (CFP)-supported nickel–iron carbonate hydroxide hydrate (NiFeCH). An aqueous solution of $Ce(NO_3)_3$ and NaCl was employed as the electrolyte, and the deposition was performed at 0.30 mA cm^{-2} for a desired duration to control the amount of Ce loading. Similarly, Zhao et al.[97] used an aqueous solution of nickel acetate and iron chloride as the electrolyte to electrodeposit FeNi alloy quantum dots (QDs) on sword-like nanoarrays of CoCH/NF. Electrodeposition was performed at 20 mA cm^{-2} for 200 s to obtain FeNi/CoCH/NF. Another recent report presented the electrodeposition of NiOOH atop Ni-foam-supported CoCu carbonate hydroxide (CoCuCH) nanorods.[98] A standard three-electrode configuration was used, where CoCuCH/NF, Ag/AgCl (saturated KCl), and a platinum plate served as the working, reference, and auxiliary electrodes, respectively. The electrodeposition was conducted in a 0.1 M aqueous solution of $Ni(NO_3)_2$ at −0.958 V for 7 min, and NiOOH@CoCuCH/NF was fabricated.

5. Structural Aspects of MTMCHs

Metal carbonate hydroxides exhibit a layered structure and have the general formula $M_x(OH)_yCO_3{\cdot}nH_2O$, where M is the metal ion in the +2 oxidation state.[75] Each layered structure is composed of ($M(OH)^+$) and intercalated anions (CO_3^{2-}).[83] The penetration of the electrolyte into the TMCH layers and the hydrophilicity of CO_3^{2-} ions in the interlayer region increase the accessibility to the active sites.[54] Despite their layered structure, the low conductivity limits the efficient electrocatalytic activity of monometallic CHs.[77] In contrast, mixed metal CHs exhibit a better OER performance than monometallic CHs owing to the synergistic interactions between various metal centers.[86] This can be attributed to the fast electron transfer and a decrease in the free energy of the RDS by increasing the electron-density near the Fermi level.[57,73] The different crystallographic phases of TMCHs are briefly discussed herein on the basis of previous reports. Wang et al.[132] reported the monoclinic crystal structure of hydrothermally synthesized $Co_2(OH)_2(CO_3)$, which was isomorphous to the naturally occurring malachite mineral group. The structural refinement via Rietveld analysis and the as-determined crystal structure are shown in **Figure 3**a,b. Accordingly, the crystal lattice of $Co_2(OH)_2(CO_3)$ consisted of Co^{2+}, CO_3^{2-}, and OH^- ions with C_1 site symmetry. There were two types of Co^{2+} and OH^- ions and one type of CO_3^{2-}. The formation of a (4 + 2) coordinated distorted octahedron was ascribed to the coordination of one type of Co^{2+} with two OH^- and two oxygen atoms from CO_3^{2-} and the coordination of another type of Co^{2+} with four OH^- and two oxygen atoms from CO_3^{2-}.[132] In contrast, Yang et al.[133] observed the formation of hydrated cobalt hydroxy carbonate $[Co(CO_3)_{0.5}(OH)\cdot 0.11H_2O]$ with an orthorhombic crystal structure, which matched well with JCPDS card No. 00-048-0083. In another study, the phase formation of cobalt hydroxide carbonate was significantly influenced by the reaction temperature. Low-temperature hydrothermal reaction (100–140 °C) resulted in an orthorhombic phase, whereas high-temperature hydrothermal reaction (≈180 °C) resulted in a monoclinic phase.[134] However, in a recent study, Bhojane et al.[135] pointed out that the previously reported $Co(CO_3)_{0.5}(OH)\cdot 0.11H_2O$ (with an orthorhombic phase) was inaccurate. They performed Rietveld refinement of the synchrotron data with Le Bail fitting of hydrothermally fabricated cobalt carbonate hydroxide hydrate and determined the chemical formula as $Co_6(CO_3)(OH)_8\cdot H_2O$ [hexacobalt(II) bis(carbonate) octahydroxide monohydrate]; the crystal structure was hexagonal (Figure 3c).[135] The corresponding findings indicate that the infinite edge-sharing $[CoO_6]$ chains following the *c* axis were interconnected by carbonate ions, as shown in Figure 3d. In another study, cubic nickel–cobalt carbonate hydroxide hydrate nanostructures were fabricated by coprecipitation; they exhibited a rhombohedral crystal structure with the chemical formula $(Ni_{6.10}Co_{2.90})(OH)_{18.27}(CO_3)_{1.315}\cdot 6.7H_2O$.[73] Therefore, the exact crystal phase and chemical formula of metal carbonate hydroxides are ambiguous and require further investigation.

6. MTMCH Electrocatalysts in Oxygen Evolution Reaction

Layered transition metal carbonate hydroxides constitute a structurally and chemically well-defined family of compounds.[55,75,83]

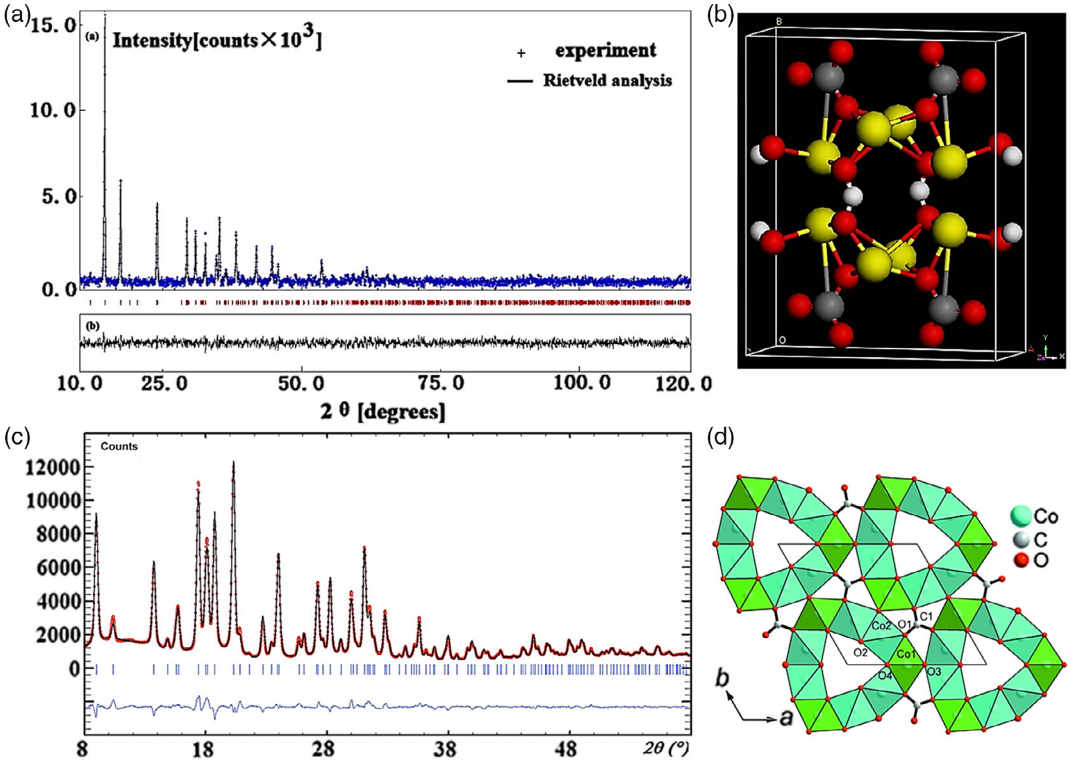

Figure 3. a) Reitveld analysis showing experimental data (blue), diffraction peak positions (red), and difference between experimental and calculated patterns and b) crystal structure of $Co_2(OH)_2(CO_3)$. Reproduced with permission.[132] Copyright 2010, Cambridge University Press. c) Refined synchrotron diffraction pattern of $Co_6(CO_3)(OH)_8\cdot H_2O$. The experimental data (red dots), calculated data (black lines), Bragg diffractions (ticks), and difference between the experimental and calculated patterns (blue curve) are represented. d) $Co_6(CO_3)(OH)_8\cdot H_2O$ unit-cell along short c axis including face/edge-sharing $[CoO_6]$ octahedra forming rings. Reproduced with permission.[135] Copyright 2019, International Union of Crystallography.

Recently, TMCHs have been investigated as electrocatalysts in alkaline water splitting and near-neutral media owing to their rich redox properties and high accessibility to electrolytes.[54,72,73] However, recent studies have reported that the poor intrinsic activity of TMCHs is a major challenge in achieving desirable OER efficiency.[74] In this context, mixed transition-metal-based carbonate hydroxides can be considered more efficient OER electrocatalysts than their monometallic counterparts. There are various modulation strategies for improving the OER kinetics and decreasing the overpotential of MTMCHs for alkaline OER.[55–57,68,72–99] **Table 1** summarizes the different approaches undertaken to achieve excellent OER performance with the good long-term stability of MTMCHs.

6.1. Compositional Tuning

Nickel–iron carbonate hydroxide hydrate (NiFeHCH) nanosheets were prepared by coprecipitation. The OER performance of nanosheets with varying Ni:Fe stoichiometric ratios (1:0.2, 1:0.4, 1:0.6, 1:0.8, and 1:1) in aqueous 1.0 M KOH and $NaHCO_3$ was investigated (**Figure 4**a).[72] The NiFeHCH (1:0.2) nanosheets demonstrated superior alkaline OER activity with a low overpotential of 250 mV at 20 mA cm^{-2} and 39 mV dec^{-1} Tafel slope (Figure 4b). The improved hydrophilicity of NiFeHCH resulted in its better OER performance than the LDH systems. This observation was confirmed by the appearance of $M - H_2O$ peak in the high-resolution O 1s spectrum, which might have increased the hydrophilicity in addition to the presence of $M - CO_2^{3-}$ bond in NiFeHCH. In another study, Karthick et al.[73] employed coprecipitation and prepared cubic nanostructures of bimetallic nickel–cobalt carbonate hydroxide hydrates (NiCoCHH) with three different Ni:Co molar ratios ranging from ≈0.5 to 1.5. The crystallinity of the NiCoCHH nanostructures changed upon varying the Ni/Co molar ratios, and the low intensity of the XRD peaks indicated the poor crystalline nature of the products due to the increase in Ni content (Figure 4c). Therefore, the Ni/Co stoichiometric ratio strongly influenced the OER activity of the cubic NiCoCHH nanostructures, and NiCoCHH (1:1) exhibited the lowest OER overpotential of ≈238 mV@10 mA cm^{-2} with 95.21% Faradaic efficiency in 1.0 M KOH. Furthermore, the post-durability test indicated surface oxidation and the appearance of NiOOH species on NiCoCHH (1:1). Yang et al.[74] reported the fabrication of partially sulfurized mesoporous nickel–iron carbonate hydroxide ultrathin nanosheets by partially replacing the carbonate and hydroxyl groups in NiFe carbonate hydroxide with S. During the synthesis, compositional optimizations were performed with different Ni:Fe molar ratios and with a controlled degree of sulfurization, the optimized Ni_2Fe_1S/CH nanosheets were obtained (Figure 4d). The modifications in the electronic structure and the partial replacement of CO_2^{3-} by S^{2-} ions were confirmed by XPS. Additionally, increasing the Fe content in Ni_xFe_yS/CH was unfavorable for alkaline OER, and Ni_2Fe_1S/CH showed a small overpotential of ≈261 mV@20 mA cm^{-2} with excellent stability (Figure 4e). The high OER performance of Ni_2Fe_1S/CH was attributed to the donor–acceptor interactions between the S^{2-} and Ni/Fe ions (which facilitated oxygen desorption), synergistic interactions of Ni and Fe centers, and a decrease in the charge transfer resistance due to the strong interactions between the sulfides and NiFeCH.

Hui et al.[55] employed a hydrothermal method and fabricated an interconnected network of vertically aligned iron–cobalt carbonate hydroxide nanosheet array on a 3D conductive Ni foam (F_xC_1CH/NF) with varying Fe/Co molar ratios. The nanosheet density increased up to a Fe/Co ratio of 0.25, and a further increase in the Fe/Co ratio resulted in thicker nanosheets and lower nanosheet densities. The strong coupling interaction and modulation of the electronic structure, caused by the introduction of Fe into cobalt carbonate hydroxide, were evident from the XPS analysis of the optimized $Fe_{0.25}C_1CH/NF$. Furthermore, density functional studies indicated that the Co center in $Fe_{0.25}C_1CH$ had more electrons in the Co 3 d orbital (Figure 4h) and higher adsorption free energies of the crucial OER intermediates (–OH, –O, and –OOH) on Co center than that in pure CCH, which are favorable for enhanced alkaline OER performance. The $Fe_{0.25}C_1CH/NF$ with an optimum Fe/Co ratio (≈0.25) required overpotentials of ≈228 and 308 mV to deliver 10 and 1000 mA cm^{-2} current densities, respectively, in alkaline OER (Figure 4f,g). This excellent performance was attributed to an increase in the electrochemical active surface area (ECSA), electron/mass transport properties, synergistic interactions, and modulation of the electronic structure through compositional tuning.

6.2. Substitution or Doping

Heteroatom substitution/doping can be considered an effective strategy for enhancing the electrocatalytic activity of TMCHs.[136,137] Doping with foreign elements or substituting the metal centers in TMCHs would lead to a strong interaction between the dopants and the matrix, thereby modifying the electronic structure of the TMCHs.[76] In particular, heterometal doping/substitution influences the electronic environment of the metal centers and regulates the population of the d-orbital electrons, which facilitates –OH adsorption on the electrocatalyst surface and improves the charge transfer. Furthermore, dopant metal atoms can also generate additional active sites for OER.[75,77,78] Such factors could be beneficial for achieving an improved OER activity in TMCHs. Elemental substitution/doping in metal carbonate hydroxides can be classified on the basis of metallic or nonmetallic dopants/substituents; the categories are discussed in the following sections.

6.2.1. Metal Substitution or Doping

Tang et al.[75] doped cobalt carbonate hydroxide (CoCH) with Mn and prepared Ni-foam-supported Co–Mn carbonate hydroxide (CoMnCH) for alkaline water splitting. Modulation of the electronic structure was evident from the XPS analysis; the Co $2p_{3/2}$ peak shifted to a lower binding energy because of Mn doping (**Figure 5**b). Further, the density of state calculations indicated that CoMnCH had a higher population of electrons in the Co 3d orbital than CoCH, which benefited the emergence of the adsorbed –OOH species on the electrocatalyst surface, thereby facilitating the oxygen evolution activity. CoMnCH showed a more significant increase in the electrocatalytic OER activity than

Table 1. Electrocatalytic OER activities of MTMCHs according to different modulation strategies.

Strategy	Materials	Synthesis	Substrate	Morphology	Electrolyte	Overpotential [mV @ 10 mA cm^{-2}]	Tafel [mV dec^{-1}]	Stability
Compositional Tuning	NiFeHCH (1:0.2)[72]	Coprecipitation	Carbon Cloth	Nanosheets	1.0 M KOH	250@20 mA cm^{-2}	39	16 h@274 mV
	NiCoCHH (1:1)[73]	Coprecipitation	Carbon Cloth	Cubic nanostructures	1.0 M KOH	238	190	12 h@324 mV
	$F_{0.25}C_1CH/NF$[55]	Hydrothermal	Nickel foam	Nanosheets array	1.0 M KOH	228	42	6000 cycles and 70 h@100 mA cm^{-2}
	NixFeyCH and NixFeyS[74]	Hydrothermal	Glassy carbon electrode	Nanosheets	1.0 M KOH	261@20 mA cm^{-2}	103	5000 cycles and 10 h@20 mA cm^{-2}
Substitution/ Doping	Co_1Mn_1CH[75]	Hydrothermal	Nickel foam	Nanosheet	1.0 M KOH	294@30 mA cm^{-2}	–	18 h@50 mA cm^{-2}
	$Co_{1.9}Ni_{0.1}(CO_3)(OH)_2/GP$[76]	Hydrothermal	Graphite paper	Rectangular Nanoplates	1.0 M KOH	266	44.8	12 h@20 mA cm^{-2}
	Co-FeNiCH/NF[77]	Hydrothermal	Nickel foam	Nanosheets	1.0 M KOH	202	37.5	20 h@1.55 V
	Fe^{3+} loaded on $Ni_2(OH)_2CO_3$[78]	Hydrothermal and immersion	Nickel foam	Microsheet-like units	1.0 M KOH	277	70	3000 cycles and 36 h@280 mV
	5%W-CCH[79]	Hydrothermal	Carbon cloth	Brush-like nanoarrays	1.0 M KOH	318	65.45	40 h@20 mA cm^{-2}
	$Cr_{0.2}$-CoCH/NF[80]	Hydrothermal	Nickel foam	Nanowires	1.0 M KOH	203	84	1000 cycles and 25 h@1.45 V
	$C@NFe_1Co_1CH/CC$[81]	Hydrothermal	carbon cloth	Nanoneedle arrays	1.0 M KOH	235	34	30 h@10 mA cm^{-2}
	N-Mn-CCH@NF[82]	Hydrothermal	Nickel foam	2D micro flakes	1.0 M KOH	318@50 mA cm^{-2}	77.2	–
Morphology Modulation	CCHS/CP[83]	Hydrothermal	Carbon Paper	Nanoneedles	1.0 M KOH	240	82.06	9 h@20 mA cm^{-2}
	CoCH[68]	Mild low-temperature precipitation	GC electrode	Nanorods	1.0 M KOH	320	38.8	5 h
	$Fe_{0.25}$–CoMoCH[57]	Hydrothermal	Ni foam	Spherical	1.0 M KOH	232	46	50 h@10 mA cm^{-2}
	Ar-plasma treated NiCo-CHs[84]	Hydrothermal	Ni foam	Nanosheets	1.0 M KOH	250	89	6000 cycles
In situ Transformation	Fe-CCHH/NF-30[85]	Hydrothermal and electrodeposition	Nickel foam	Nanowires	1.0 M KOH	200	50	130 h@55 mA cm^{-2}
	Partially sulfurated CoFeCHs[56]	Hydrothermal	Nickel foam	Nanosheet and porous structure	1.0 M NaOH	226 367@1000 mA cm^{-2}	41.3	100 h@50 mA cm^{-2}
	Co_xNi_yCH[86]	Hydrothermal	Ni foam	Nanosheets	1.0 M KOH	256@50 mA cm^{-2}	51	18 h@50 mA cm^{-2}
Hybrid/ Heterostructures	$Cu(OH)_2$@CCHH/CF[87]	Chemical bath deposition	Copper foam	Nanowire	1.0 M KOH	290@100 mA cm^{-2}	78	1000 cycles and 20 h@260 mV
	$Cu(OH)_2$@CoNiCH/CF[88]	Hydrothermal	Copper foam	Nanotubes	1.0 M KOH	288@30 mA cm^{-2}	74	1000 cycles and 12 h@10 mA cm^{-2}
	PBA@ CoHC/CC[89]	Hydrothermal	Carbon cloth	Cube	1.0 M KOH	240	79	50 h@1.5 V
	FeOOH/NiFe LDHs@CCH/NF[90]	Hydrothermal	Nickel foam	Nanoplates	1.0 M KOH	220	–	40 h@multistep 10–500 mA cm^{-2}
	P-$NiMoO_4$@CoCH/CC[91]	Hydrothermal	Carbon Cloth	Nanosheet	1.0 M KOH	267@40 mA cm^{-2}	99	20 h
	CH@NCHC-Pd /CF[92]	Hydrothermal	Copper foam	Nanothorn–Nanotube arrays	1.0 M KOH	136	64	1000 cycles and 12 h
	NiFeCH(Ce)[93]	Hydrothermal & electrodeposition	Carbon fiber paper	Nanosheet	1.0 M KOH	252@100 mA cm^{-2}	59	48 h
	$Ni_{0.75}Fe_{0.15}Ce_{0.10}/NF$[94]	Hydrothermal	Nickel foam	Nanosheets	1.0 M KOH	228	38.3	46 h@10 mA cm^{-2}
	CFMS@CFOC/[95]	Hydrothermal	Ti mesh	Nanowires	1.0 M KOH	237	118	25 h@290 mV
	Cu_3N@CoNiCHs@CF[96]	Hydrothermal	Copper foam	Nanothorns	1.0 M KOH	155	96	3000 cycles and 24 h @1.38 V

Table 1. Continued.

Strategy	Materials	Synthesis	Substrate	Morphology	Electrolyte	Overpotential [mV @ 10 mA cm^{-2}]	Tafel [mV dec^{-1}]	Stability
	FeNi/CoCH/NF[97]	Hydrothermal & electrodeposition	Nickel foam	Sword-like nanoarrays	1.0 M KOH	240@20 mA cm^{-2}	44.8	2000 cycles and 23 h
	NiOOH@CoCu CH[98]	Hydrothermal & electrodeposition	Nickel foam	Nanorods	1.0 M KOH	263	43.2	22 h@1.46 V
	NiFe-MOF/FeCH-NF[99]	Hydrothermal	Nickel foam	Nanosheets	1.0 M KOH	200	51.3	50 h@10 mA cm^{-2}

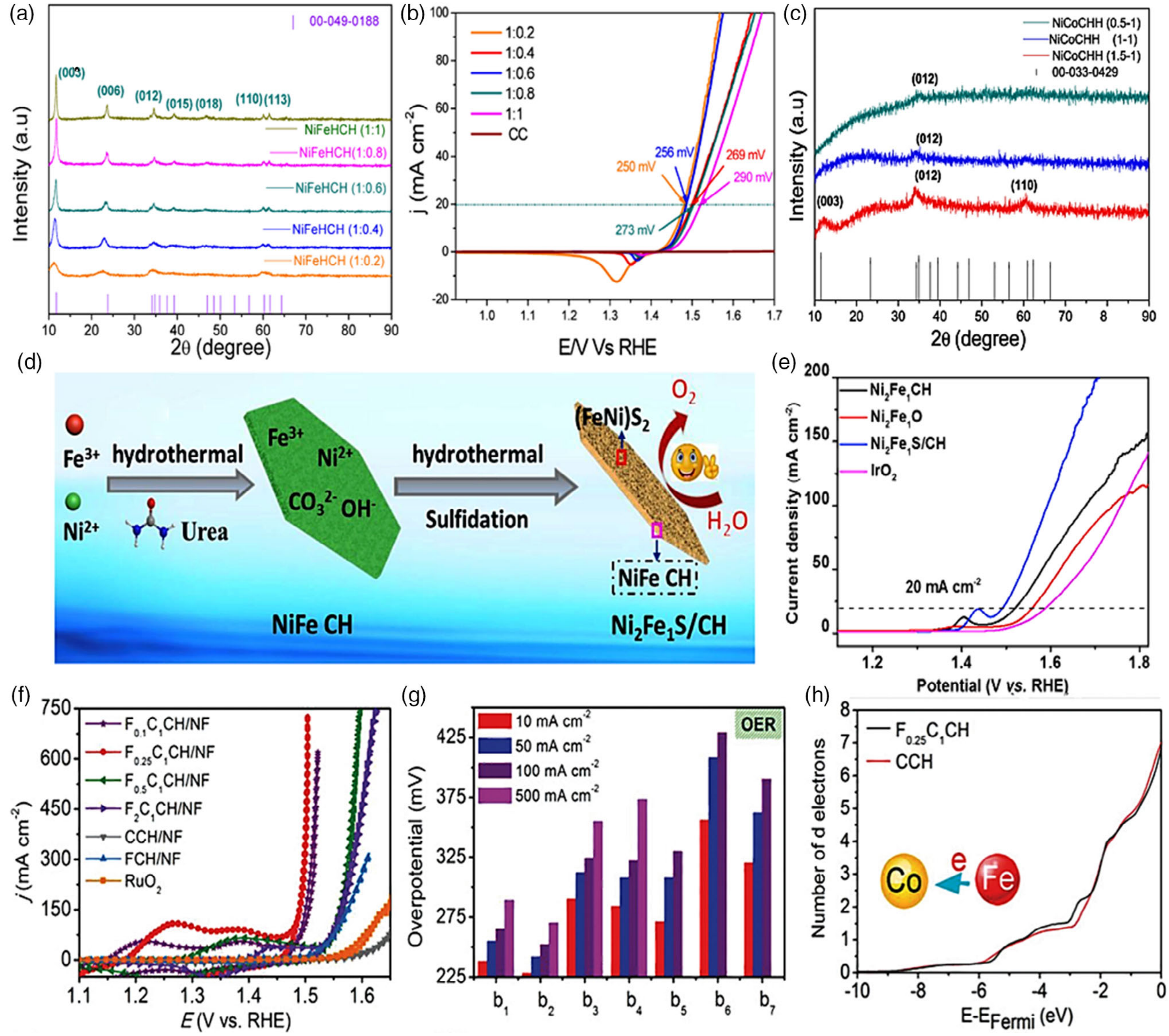

Figure 4. a) XRD patterns and (b) reverse cyclic voltammetry (CV) (scan rate: 1 mV s^{-1}) in 1.0 M KOH of NiFeHCH nanosheets with different Ni/Fe ratios. Reproduced with permission.[72] Copyright 2019, American Chemical Society. c) XRD patterns of NiCoCHH with various Ni/Co molar ratios. Reproduced with permission.[73] Copyright 2020, American Chemical Society. (d) Schematic representation of the preparation procedure and e) LSV curves for OER in 1.0 M KOH of Ni_xFe_yS/CH nanosheets. Reproduced with permission.[74] Copyright 2019, Elsevier Ltd. f) CV and g) OER overpotentials of b_1-$F_{0.1}C_1CH/NF$, b_2-$F_{0.25}C_1CH/NF$, b_3-$F_{0.5}C_1CH/NF$, b_4-F_2C_1CH/NF, b_5-CCH/NF, b_6-FCH/NF, and b_7-RuO_2. h) 3 d orbital electron count per Co atom in CCH and $F_{0.25}C_1CH$. Reproduced with permission.[55] Copyright 2018, Wiley-VCH GmbH.

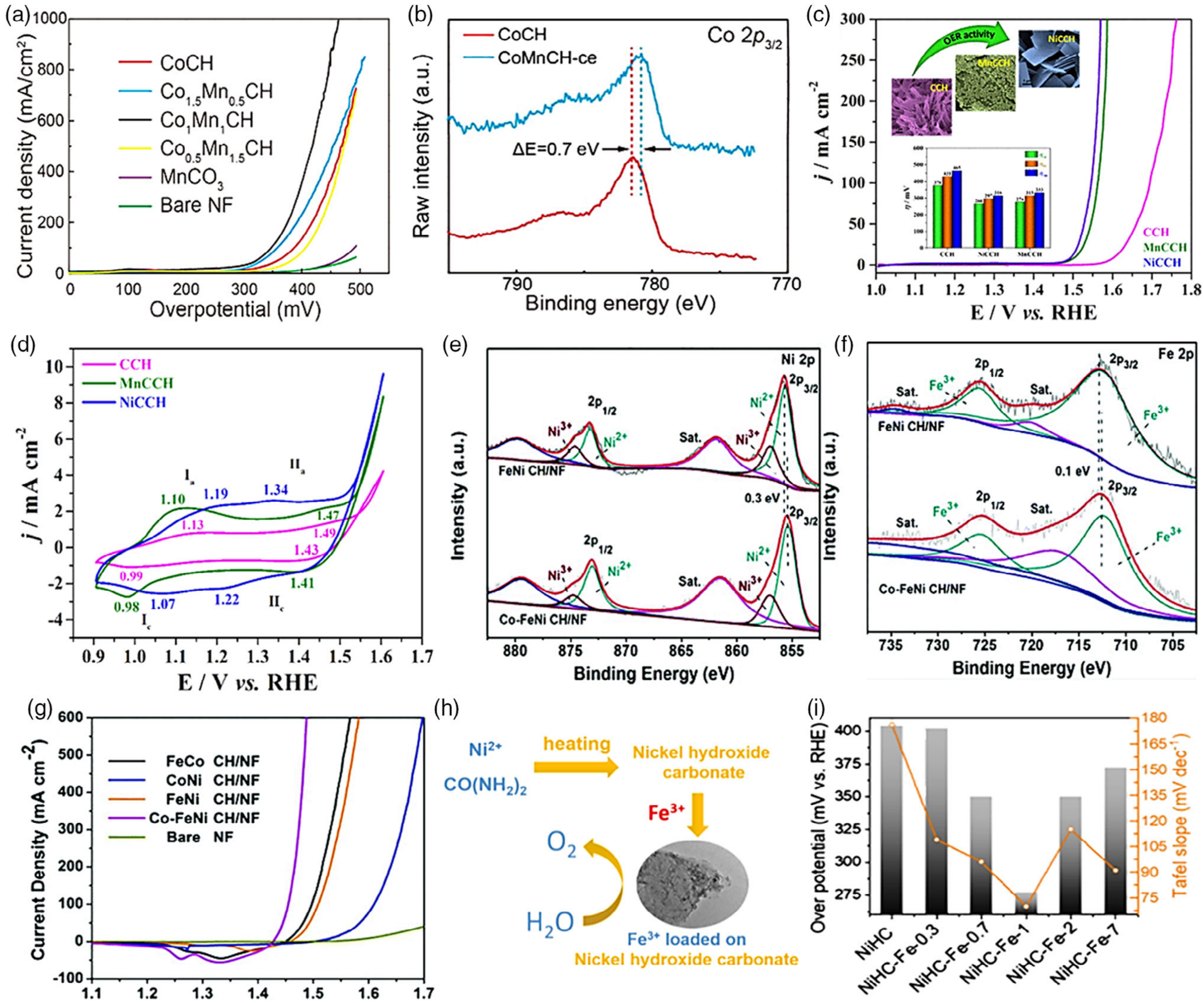

Figure 5. a) *iR*-corrected LSV polarization curve at 5 mV s^{-1} for OER of Co$_x$Mn$_y$CH samples and bare NF in 1.0 M KOH. b) High-resolution Co 2p$_{3/2}$ XPS spectra of CoCH and CoMnCH-ce. Reproduced with permission.[75] Copyright 2017, American Chemical Society. c) OER Polarization curves (*iR*-corrected) at 5 mV s^{-1} of NiCCH, MnCCH, and CCH. The insets show morphology and overpotentials at different current densities. d) CV without *iR*-correction at 10 mV s^{-1} of NiCCH, MnCCH, and CCH for OER mechanism exploration. Reproduced with permission.[76] Copyright 2020, American Chemical Society. Comparison of the deconvoluted e) Ni 2p and f) Fe 2p X-Ray photoelectron spectroscopy (XPS) spectra of Co-FeNiCH/NF and/or FeNiCH/NF samples. g) LSV curves for OER of Co-FeNiCH/NF, FeCoCH/NF, FeNiCH/NF, CoNiCH/NF, and bare NF. Reproduced with permission.[77] Copyright 2019, The Royal Society of Chemistry. h) Synthetic scheme and i) comparison of OER overpotential and Tafel slope values of different Fe^{3+}-loaded Ni$_2$(CO$_3$)(OH)$_2$ samples. Reproduced with permission.[78] Copyright 2020, Elsevier.

CoCH; it required an overpotential of 294 mV to deliver 30 mA cm^{-2} current density (Figure 5a). In addition, the morphological modulation of the nanosheet arrays and the compact structure grown on Ni foam helped CoMnCH to achieve 1000 mA cm^{-2} current density at an overpotential of 462 mV. The effect of Co substitution with Ni and Mn was studied in GP-supported Co$_2$(CO$_3$)(OH)$_2$ (CCH) nanostructures for the alkaline OER (Figure 5c).[76] The Ni and Mn substitutions were effective in modulating the crystal structure, morphology, and electronic structure and increased the ECSA significantly. The substituted Co$_{1.9}$Ni$_{0.1}$(CO$_3$)(OH)$_2$/GP (NiCCH) and Co$_{0.95}$Mn$_{0.05}$CO$_3$/GP (MnCCH) exhibited better OER performance than pure CCH and also commercial RuO$_2$ electrocatalyst in 1.0 M KOH. NiCCH required only 266 mV overpotential to reach 10 mA cm^{-2} current density and exhibited considerably fast OER kinetics with a low Tafel slope of ≈44.8 mV dec^{-1}. Ni substitution was more effective in decreasing the OER overpotential than Mn substitution. Furthermore, the electrochemical analysis of the OER mechanistic pathways identified the Co^{3+}-to-Co^{4+} oxidation as the RDS (Figure 5d); Ni facilitated the RDS owing to its higher electronegativity than Mn.

Qi et al.[77] grew a Co-doped FeNi carbonate hydroxide nanosheet array on Ni foam (Co–FeNiCH/NF) via a one-step hydrothermal method. In the XPS spectra, the Fe 2p, Ni 2p, and O 1s peak positions in Co–FeNiCH/NF were redshifted relative to those in FeNiCH/NF, indicating the successful incorporation of Co and the modification of the electronic structure (Figure 5e,f). The Co–FeNiCH/NF exhibited an overpotential of ≈202 mV at 10 mA cm^{-2} (Figure 5g), a Tafel slope of 37.5 mV dec^{-1}, and good durability (20 h) in the alkaline OER. The significantly increased ECSA and decreased electron transfer resistance accounted for the enhanced performance. Further, it was assumed that Co doping helped to improve the OER performance by optimizing the electron affinity of the active centers for –OH adsorption and rapid charge transfer. The postmortem analysis of Co–FeNiCH/NF after OER stability identified M–OOH as the main OER active species, which was inferred from the increased Ni^{3+}/Ni^{2+} photoelectron peak ratio.

Low-crystalline $Ni_2(CO_3)(OH)_2$ loaded with Fe^{3+} (NiHC-Fe) was fabricated using a hydrothermal method followed by a simple immersion procedure (Figure 5h).[78] The Fe^{3+} loading was guided by the difference in the K_{sp} values of $Ni(OH)_2$ and $Fe(OH)_3$. In addition, the Fe^{3+} content was optimized; NiHC-Fe-1, obtained after immersion in 1 M Fe^{3+} aqueous solution, demonstrated the highest alkaline OER activity with 277 mV overpotential at 10 mA cm^{-2} and a Tafel slope of 70 mV dec^{-1} (Figure 5i). It was postulated that Fe would promote the conversion of Ni sites to higher oxidation states, which would favor the proper binding of OER intermediates. In addition, the introduction of Fe into NiHC led to the emergence of Fe–O–Ni species as additional active sites. Thus, the effective synergistic interaction between the Fe and Ni centers imparted high oxygen evolution activity to NiHC-Fe-1. Jin et al.[79] synthesized W-doped cobalt hydroxide carbonate (W-CCH) brush-like nanoarrays on carbon cloth (CC) with varying atomic percentage (at.%) of the W dopant (**Figure 6**a) using a hydrothermal route. The doping concentration of W^{6+} was optimized to 5 at% in terms of the OER performance in 1.0 M KOH electrolyte. The optimum 5%W-CCH required a much lower OER overpotential (318 mV) to deliver 10 mA cm^{-2} current density than CCH (332 mV) (Figure 6c). In contrast, W-CCH exhibited a lower ECSA with increasing W content than CCH, suggesting that high intrinsic activity was a dominant factor (instead of an increase in the electroactive surface area) in W-CCH for improved OER performance. Furthermore, a more detailed analysis revealed an increase in the electron density near the Fermi level due to the 5 at%

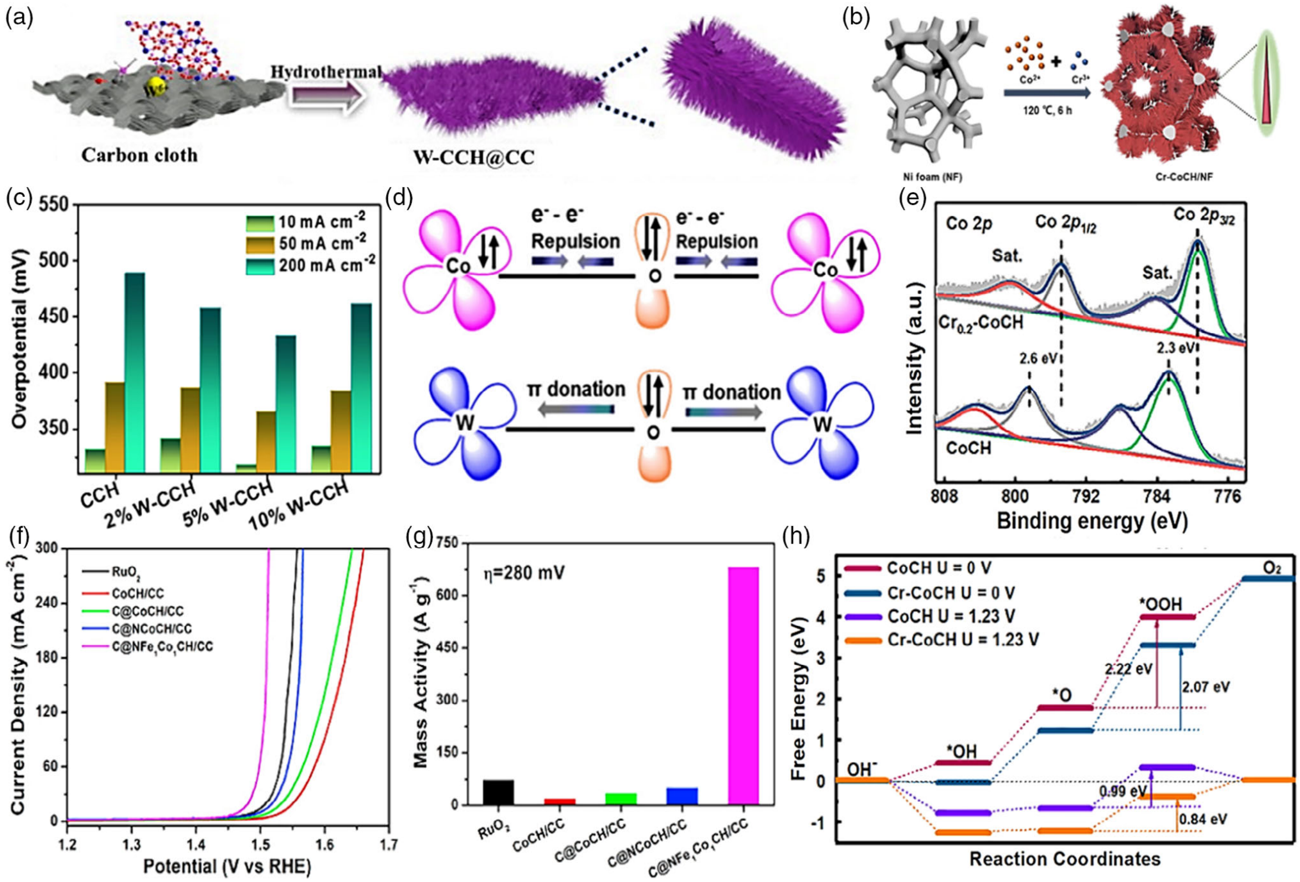

Figure 6. a) Schematic representation of the preparation and (c) overpotentials needed at current densities ranging from 10 to 200 mA cm^{-2} of CCH and W-CCH. (d) Schematic illustration of the electronic coupling between Co and W in W-CCH. Reproduced with permission.[79] Copyright 2020, Elsevier. b) Proposed fabrication scheme of Cr_x-CoCH (x = 0, 0.1, 0.2, 0.4) and e) high resolution Co 2p XPS spectra of $Cr_{0.2}$-CoCH and CoCH. h) Calculated free energy diagram for the OER on Cr-CoCH and CoCH. Reproduced with permission.[80] Copyright 2021, Elsevier. f) OER polarization curves @ 2 mV s^{-1} and (g) mass activities at the $\eta = 280$ mV of RuO_2, CoCH/CC, C@CoCH/CC, C@NCoCH/CC, and $C@NFe_1Co_1CH/CC$ in 1.0 M KOH. Reproduced with permission.[81] Copyright 2019, Elsevier.

W^{6+} doping; the dopants also acted as O_2^- adsorption sites. W doping was also effective in enhancing the OER activity of various metal carbonate hydroxides with greater than or equal to half-filled metal d-orbitals (Figure 6d). In a recent study, Zhao et al.[80] doped Ni-foam-supported CoCH nanowire arrays (Figure 6b) with Cr to modify their morphology, electronic structure (Figure 6e), ECSA, and electrocatalytic OER activity in 1.0 M NaOH. The optimal $Cr_{0.2}$-CoCH/NF exhibited the highest ECSA and a considerable improvement in the OER performance with a lower overpotential (≈203 mV@10 mA cm^{-2}) than undoped CoCH/NF (273 mV). The theoretical investigation of the OER mechanism identified *OOH formation as the RDS, and Cr doping decreased the energy barrier of the RDS, thereby boosting the OER activity in 1.0 M NaOH (Figure 6h).

In contrast, doping of very small or ultralow amount of noble metals, such as Ru and Ir into TM-based oxides, hydroxides, and LDHs also evidenced as an effective modulation strategy to enhance OER activity.[138–142] The advantages of ultralow noble metal doping include adsorption energy optimization of OER intermediates on the electrocatalyst surface through electronic structure modulation, acting as additional active sites, increase in electrical conductivity, and active surface areas by inducing lattice distortion.[143–145] These factors highly facilitate the OER kinetics and decrease the overpotential. For example, Li et al.[146] reported enhanced OER performance of ultralow Ir-doped $Co(OH)_2$ nanosheets, fabricated by a facile cation-exchange reaction. The synergistic interaction between the Ir and $Co(OH)_2$ resulted in high intrinsic oxygen evolution activity in the electrocatalyst by regulating the adsorption energy of the OER intermediates. Further, this approach was also highlighted as a universal method for Ir-doping in a series of Co-based bimetallic LDHs. However, there are no studies available on noble metal doping in MTMCHs for electrocatalytic OER applications.

6.2.2. Nonmetal Doping

Dai et al.[81] used a hydrothermal route and low-temperature calcination to fabricate thin carbon-coated N/Fe-modified CCH needle arrays on carbon cloth (C@NFeCoCH/CC) and studied its electrochemical performance in the alkaline OER. The introduction of Fe into CoCH modified the electronic structure of the Co centers, and among the different Fe/Co ratios, $C@NFe_1Co_1CH/CC$ showed the lowest OER overpotential (Figure 6f). $C@NFe_1Co_1CH/CC$ (optimal composition) demonstrated an overpotential of ≈235 mV@10 mA cm^{-2}, mass activity of 681.4 A g^{-1}, and stability over 30 h at 10 mA cm^{-2} (Figure 6g). The N doping and the thin carbon layer boosted the oxygen evolution ability by forming Co/Fe–N–C species as well as enhanced the conductivity. The conductive carbon cloth, thin carbon layer, and N/Fe modification in $C@NFe_1Co_1CH/CC$ resulted in a stable, fast charge transfer between the interface and the electrolyte. Recently, Wang et al.[82] derived N and Mn dual-doped cactus-like Co_3O_4 nanostructures from cobalt carbonate hydroxides (CCH) and grew them on Ni foam using N_2 plasma. In their study, the time for the hydrothermal reaction was first optimized to 6 h to achieve superior OER performance of the Mn-CCH@NF precursor. The subsequent treatment with N_2 plasma at room temperature led to the formation of N-doped Mn-CCH@NF and atomic defects/vacancies, which enhanced its intrinsic activity and electronic conductivity. N-Mn-CCH exhibited a lower OER overpotential (≈318 mV @ 50 mA cm^{-2}) than Mn-CCH (≈327 mV) in 1.0 M KOH.

6.3. Morphological Modulations

Zhang et al.[83] prepared nanoneedle-assembled 3D CCH superstructures via hydrothermal synthesis; the superstructures exhibited an enhanced OER performance with an overpotential of ≈240 mV@10 mA cm^{-2} (**Figure 7**a,b). The enhancement was ascribed to the rough surface of the ordered 3D assembled superstructure, improved ECSA, and active-site accessibility. In another report, the η_{10} and Tafel slope of the CCH nanorods were ≈320 mV and 39 mV dec^{-1}, respectively.[68] Cai et al.[57] demonstrated that FeCoMo/CoMo carbonate hydroxide core–shell microspheres were promising electrocatalysts ($\eta_{10} = 232$ mV) for the OER in alkaline media (Figure 7c,d). The presence of Fe in the core resulted in energy level modulation, thereby shifting the valence band of $Fe_{0.25}$–CoMoCH closer to the thermodynamic potential (1.23 V) for the OER than that of CoMoCH (Figure 7e). In addition, the amorphous structure of $Fe_{0.25}$–CoMoCH facilitated oxygen evolution activity owing to numerous active centers and high ECSA.

In another study, Ar plasma was used for exfoliating NiCo carbonate hydroxide nanowires into nanosheets, leading to the formation of a 3D dendritic structure, as shown in Figure 7f–k).[84] This Ar plasma exfoliation strategy was instrumental in enhancing the specific surface area and ECSA, thereby improving the OER activity with 250 mV@10 mA cm^{-2} and 89 mV dec^{-1} Tafel slope. Furthermore, a population of higher oxidation states of Ni and Co was also observed as a result of the plasma treatment, which promoted the diffusion of the analytes and accelerated the charge transfer at the electrode–electrolyte interfaces.

6.4. In Situ Transformations

Zhang et al.[85] synthesized Fe-doped cobalt carbonate hydroxide hydrate nanowires grown on nickel foam (Fe-CCHH/NF) via a hydrothermal treatment followed by an in situ electrochemical modification (**Figure 8**a). The Fe doping concentration was optimized by performing in situ electrochemical transformation for different time intervals; Fe-CCHH/NF-30, obtained after 30 min of electrolysis, exhibited the best OER performance. The modification of the electronic environment and the coordination nature around the Co centers were evidenced by the XPS and EXAFS analyses (Figure 8d,e) of Fe-CCHH/NF, respectively. Further, DFT investigations indicated that the increase in the electron density of the Co 3d orbital favored the formation of –OOH intermediate, which enhanced the OER in alkaline media (Figure 8f,g). The optimized Fe-CCHH/NF-30 exhibited a small OER overpotential of ≈200 mV@10 mA cm^{-2}, a Tafel slope of ≈50 mV dec^{-1}, and an excellent stability for 130 h at 55 mA cm^{-2} in 1.0 M KOH (Figure 8b,c). To achieve high OER performance and excellent durability, Tang et al. adopted an in situ approach.[56] They fabricated a metal-sulfide–metal-carbonate hydroxide heterostructure (Figure 8h), wherein the heterointerface was obtained by partially sulfurizing the CoFe carbonate

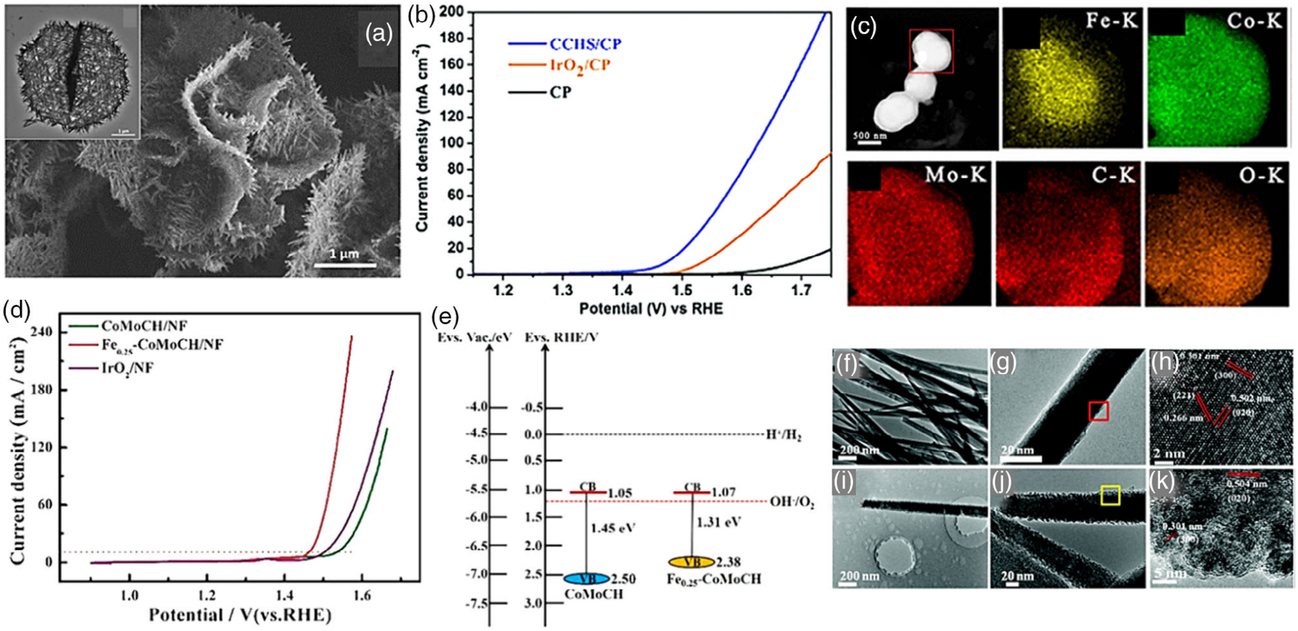

Figure 7. a) FESEM and TEM images of cobalt carbonate hydroxide superstructures on carbon paper (CCHS/CP) and (b) OER polarization curves of CCHS/CP, CP, and IrO_2/CP. Reproduced with permission.[83] Copyright 2017, The Royal Society of Chemistry. c) HAADF-STEM and corresponding elemental mapping images of $Fe_{0.25}$—CoMoCH. d) LSV curves for OER of CoMoCH/NF, $Fe_{0.25}$—CoMoCH/NF, and IrO_2/NF. e) Comparison of band gap structure of CoMoCH and $Fe_{0.25}$—CoMoCH. Reproduced with permission.[57] Copyright 2019, American Chemical Society. TEM and HRTEM images of NiCo-LDHs (f,g, and h) and 10 min Ar-plasma treated NiCo-LDHs (i, j, k). Reproduced with permission.[84] Copyright 2019, The Royal Society of Chemistry.

hydroxide nanoarrays on Ni foam. The partial sulfurization was more instrumental in decreasing the OER overpotential than complete sulfurization. The CoFe carbonate hydroxide/sulfide with a nanoparticle-in-nanosheet morphology exhibited an overpotential of ≈226 mV@10 mA cm^{-2} and delivered an industrial standard current density of ≈1 A cm^{-2} at merely 367 mV overpotential in the alkaline OER. It was assumed that the metal–S/CH heterointerface enhanced the intrinsic activity via electronic-structure modulation by transferring electrons from the M–S antibonding orbital to the M–O bonding orbitals. Recently, Liu et al.[86] identified in situ metal oxyhydroxides, which originated from the partial phase transformation of Co_xNi_yCH holey nanosheet arrays, as the real active species in alkaline OER. The emergence of electrocatalytically active CoOOH and NiOOH species during the OER was evidenced by the increase in the Co^{3+}/Co^{2+} and Ni^{3+}/Ni^{2+} ratios of Co_xNi_yCH on comparing the XPS spectra (before and after OER). Further, they pointed out that the small Fe impurities in the electrolyte (1.0 M KOH) played a key role in assisting the phase transition, thereby preventing the dissolution of Co in the alkaline solution during electrolysis and improving the electronic conductivity of the electrocatalyst. Thus, Co_xNi_yCH was proven to be an efficient precatalyst ($\eta_{50} \approx 256$ mV and Tafel slope = 51 mV dec^{-1}) for the OER in the presence of Fe-containing alkaline media (Figure 8i,j).

6.5. Hybrid Structures or Heterostructures

Hybrid structures or heterostructures of mixed-metal-based electrocatalysts can be beneficial in terms of synergistic interactions, 3D structures, heterointerfaces, and numerous available electrochemical active sites.[147–149] Xie et al.[87] investigated the alkaline OER performance of Cu-foam-supported $Cu(OH)_2$@CCHH core–shell hybrid nanowire arrays ($Cu(OH)_2$@CCHH NW/CF) fabricated via a wet-chemical approach (**Figure 9**a). The large surface area, many exposed active sites, high charge-transfer rate, and rapid electrode kinetics of the Cu-foam-supported $Cu(OH)_2@CoCO_3(OH)_2{\cdot}nH_2O$ core–shell nanowire arrays accounted for its low overpotential of ≈270 mV@50 mA cm^{-2} in 1.0 M KOH (Figure 8b). Alternatively, the hierarchical nature of $Cu(OH)_2$@CCHH NW/CF and the synergism between the $Cu(OH)_2$ core/$CoCO_3(OH)_2{\cdot}nH_2O$ shell were instrumental in enhancing the OER activity.

In another study, Kang et al.[88] also used directly grown $Cu(OH)_2$ nanotubes on Cu foam ($Cu(OH)_2$ NTs/CF) as the substrate and grew CoNiCH nanothorns atop the substrate to form core–shell $Cu(OH)_2$@CoNiCH NTs/CF (Figure 9c–f). This hybrid structure showed better hydrophilicity than $Cu(OH)_2$ NTs/CF. The 3D hierarchical core–shell $Cu(OH)_2$@CoNiCH nanotubes on Cu foam exhibited an overpotential of ≈288 mV@30 mA cm^{-2} in the alkaline OER. The authors suggested that a large surface area and the presence of several mesoporous/short diffusion paths could increase the number of available active sites. In addition, better OER performance could be attributed to a faster electron transport. Indra et al.[89] used CC-supported cobalt hydroxide carbonate (CoHC/CC) as a template to fabricate cubic Prussian blue analogs (PBAs), forming a heterostructure of PBA@CoHC/CC. The CCH/CC template was essential for effectively decreasing the OER overpotential of the templated PBAs relative to that of the PBAs without any template.

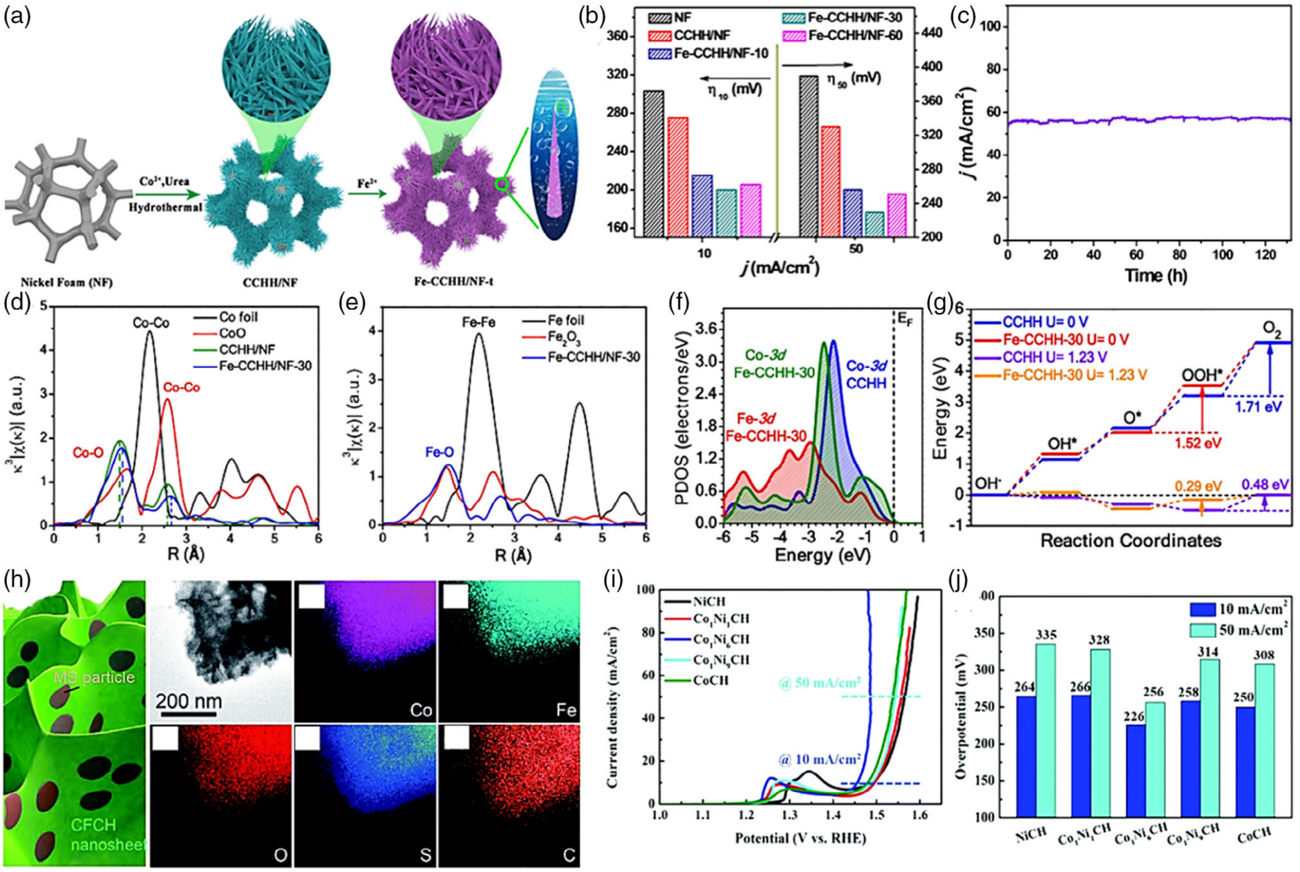

Figure 8. a) Fabrication scheme of the Fe-CCHH/NF-*t* (*t* represents time). b) Overpotential of Fe-CCHH/NF-*t* samples, CCHH/NF, and bare NF. c) Long-term stability of Fe-CCHH/NF-30 for 130 h @ 55 mA cm^{-2}. d,e) FT-EXAFS of the CCHH/NF, Fe-CCHH/NF-30, and the reference samples. f) Projected density of states and g) reaction free energy diagram for OER of CCHH and Fe-CCHH-30. Reproduced with permission.[85] Copyright 2020, American Chemical Society. h) Schematic representation and the EDX elemental mapping images of partial sulfurated CFCH (psCFCH). Reproduced with permission.[56] Copyright 2019, The Royal Society of Chemistry. i) LSV curves and j) overpotentials (at 10 and 50 mA cm^{-2}) for OER of different Co$_x$Ni$_y$CH samples. Reproduced with permission.[86] Copyright 2022, The Royal Society of Chemistry.

The templated sample (designated t-Co^{II}-Co^{III}) exhibited a low OER overpotential (η_{10}) of ≈240 mV in a 1.0 M aqueous KOH solution. The post-OER detailed spectroscopic and microscopic characterizations revealed the electrochemical transformation of PBA into a hydroxide–oxyhydroxide structure and the disappearance of the –CN group during the alkaline OER. The formation of an integrated system with a strong electrocatalyst support, improved charge transfer, and availability of a greater number of active centers were presumed to be responsible for such high OER performance. A multicomponent hierarchical hybrid comprising FeOOH/NiFe LDH nanoplates grown atop the CCH nanowire arrays on NF (Figure 9g), prepared via a two-step hydrothermal synthesis, was an effective OER electrocatalyst with low overpotential (η_{10}) of ≈220 mV in 1.0 M KOH.[90] Such a hierarchical construction was intended to increase the surface area for improving the electrolyte accessibility and mass transport during the OER. Wang et al.[91] constructed a 3D hybrid composed of P-doped NiMoO$_4$ (NiMoP) parallel nanosheets on CC-supported CoCH nanowire arrays (Figure 9i), which showed good alkaline OER activity (267 mV@40 mA cm^{-2}). The high electrochemical activity of 3D NiMoP@CoCH/CC possibly resulted from the synergism of NiMoP and CoCH, which formed quasi-1D channels and enhanced the electrolyte penetration. The oxygen vacancies (introduced during the phosphorization) and the P dopant might also have been instrumental in enhancing the electronic conductivity as well as the intrinsic electrocatalytic activity. Kang et al.[92] demonstrated a prospective approach for achieving an ultralow OER overpotential of ≈207 mV@100 mA cm^{-2}. They employed a 3D integrated precious-metal (Pd)-decorated hybrid structure of a core/shell electrocatalyst comprising a Cu(OH)$_2$ NTs/CF core and a nickel–cobalt hydroxide carbonate (NCHC) nanothorn shell (Figure 9h,j). The Tafel analysis identified OH$^-$ adsorption and O–H bond-breaking steps as the RDS in the alkaline OER for CH@NCHC-Pd NT/CF (64 mV dec^{-1}). Cu(OH)$_2$ NTs/CF exhibited poor OER performance; however, its role was crucial in improving the oxygen evolution ability of the CH@NCHC-Pd NT/CF hybrid. The high electrolyte exposure of the active sites was attributed to the large surface area imparted by the nanotubes and the hierarchical morphology of the hybrid. Additionally, the improved electrode wettability, due to the presence of OH$^-$ and CO$_3^{2-}$, boosted the OER activity. The

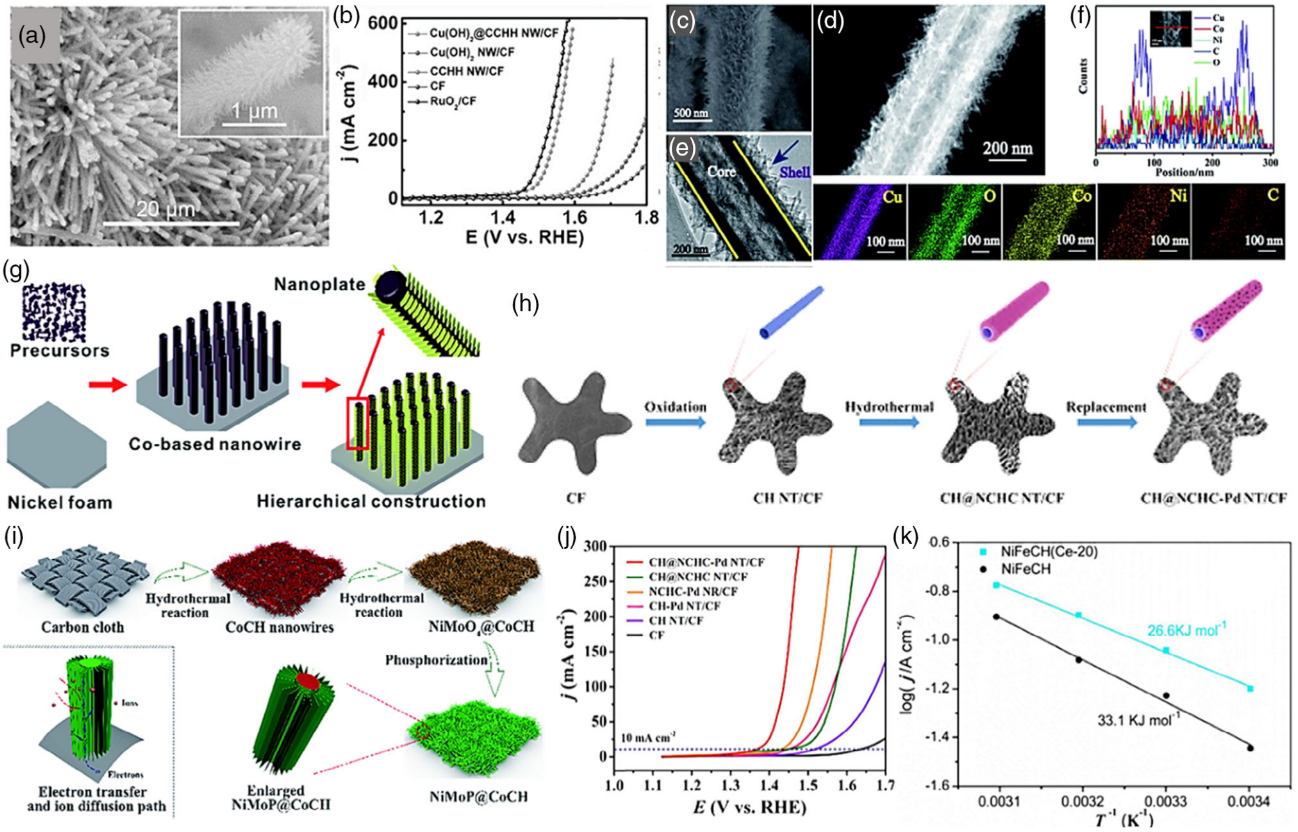

Figure 9. a) SEM images of $Cu(OH)_2$@CCHH NW/CF and (b) OER polarization curves of bare CF, RuO_2/CF, $Cu(OH)_2$ NW/CF, and $Cu(OH)_2$@CCHH NW/CF. Reproduced with permission.[87] Copyright 2017, Wiley-VCH GmbH. (c) High magnification SEM image, (d) HAADF-STEM image, e) high-magnification TEM image, f) HAADF line-scan and corresponding elemental mapping images for Cu, Co, Ni, C, and O of $Cu(OH)_2$@CoNiCH NTs. Reproduced with permission.[88] Copyright 2018, The Royal Society of Chemistry. (g) Synthetic scheme for the FeOOH/NiFe-LDHs@CCH NAs-NF. Reproduced with permission.[90] Copyright 2018, The Royal Society of Chemistry. h) Schematic illustration of the formation of 3D CH@NCHC-Pd NT/CF electrode and j) Polarization curves of CH@NCHC-Pd NT/CF, CH@NCHC NT/CF, NCHC-Pd NR/CF, CH-Pd NT/CF, CH NT/CF, and bare CF in 1.0 M KOH. Reproduced with permission.[92] Copyright 2019, American Chemical Society. i) Schematic representation of the preparatory pathways of the NiMoP@-CoCH/CC hybrid and the pathways for the electrons transfer and ions diffusion in the NiMoP parallel nanosheet architecture. Reproduced with permission.[91] Copyright 2019, The Royal Society of Chemistry. k) Arrhenius plots of NiFeCH and NiFeCH (Ce-20) for activation energy determination. Reproduced with permission.[93] Copyright 2019, Springer-Verlag GmbH Germany.

heterostructure prepared by electrodepositing CeO_x on CFP-supported nickel–iron carbonate hydroxide hydrate nanosheets (NiFeCH(Ce)) delivered a high current density of $\approx$100 mA cm^{-2} at a low overpotential of $\approx$252 mV in the alkaline OER.[93] The introduction of CeOx induced a strong electronic interaction between Ce and Ni atoms, which was evident from the shifting of Ni 2p photoelectron peaks and Ni^{3+} ions were also identified as the OER active sites from the XPS analysis. Adding to this, CeO_x incorporation also made NiFeCH(Ce) oxygen-vacancy-rich, which was beneficial for modifying the coordination environment and electrical conductivity. Furthermore, the temperature-dependent OER activity indicated that the NiFeCH(Ce) heterostructure had a lower activation energy (E_a) barrier than NiFeCH (Figure 9k). Therefore, the strong electronic interactions, enriched oxygen vacancies, and increased population of active Ni^{3+} sites contributed to the high OER performance of NiFeCH(Ce). In another study, in situ modified $CeCO_3OH$–NiFe-LDH 3D hybrid grown on Ni foam was investigated for the OER (**Figure** **10**a).[94] $CeCO_3OH$ effectively promoted the OER activity of the hybrid owing to the high oxophilicity of $Ce(OH)_3$, which accelerated OH^- adsorption and O_2 desorption. In addition, the in situ oxidation of Ce^{3+} to Ce^{4+} during the OER and the modification of the electronic environment around Ni and Fe due to the prominent electronic interaction of Ce with NiFe-LDH facilitated the binding of the OER intermediates on the electrocatalyst surface. Furthermore, the increased hydrophilicity, owing to the presence of CO_3^{2-} ions, was also instrumental in enhancing the electrolyte exposure and optimizing the oxygen intermediate binding. A possible mechanistic pathway for the OER over the $CeCO_3OH$/NiFe LDH hybrid is schematized in Figure 10b. Thus, the synergistic interaction of $CeCO_3OH$ and NiFe-LDH resulted in the high alkaline OER activity ($\eta_{10} \approx$ 228 mV) and small Tafel slope (38.3 mV dec^{-1}) of the hybrid $Ni_{0.75}Fe_{0.15}Ce_{0.10}$/NF.

According to previous studies, introducing a heterointerface of crystalline and amorphous components can be a feasible approach to superior electrocatalytic activity.[150,151] Zhao et al.[95] adopted this strategy and fabricated a 3D heterostructure

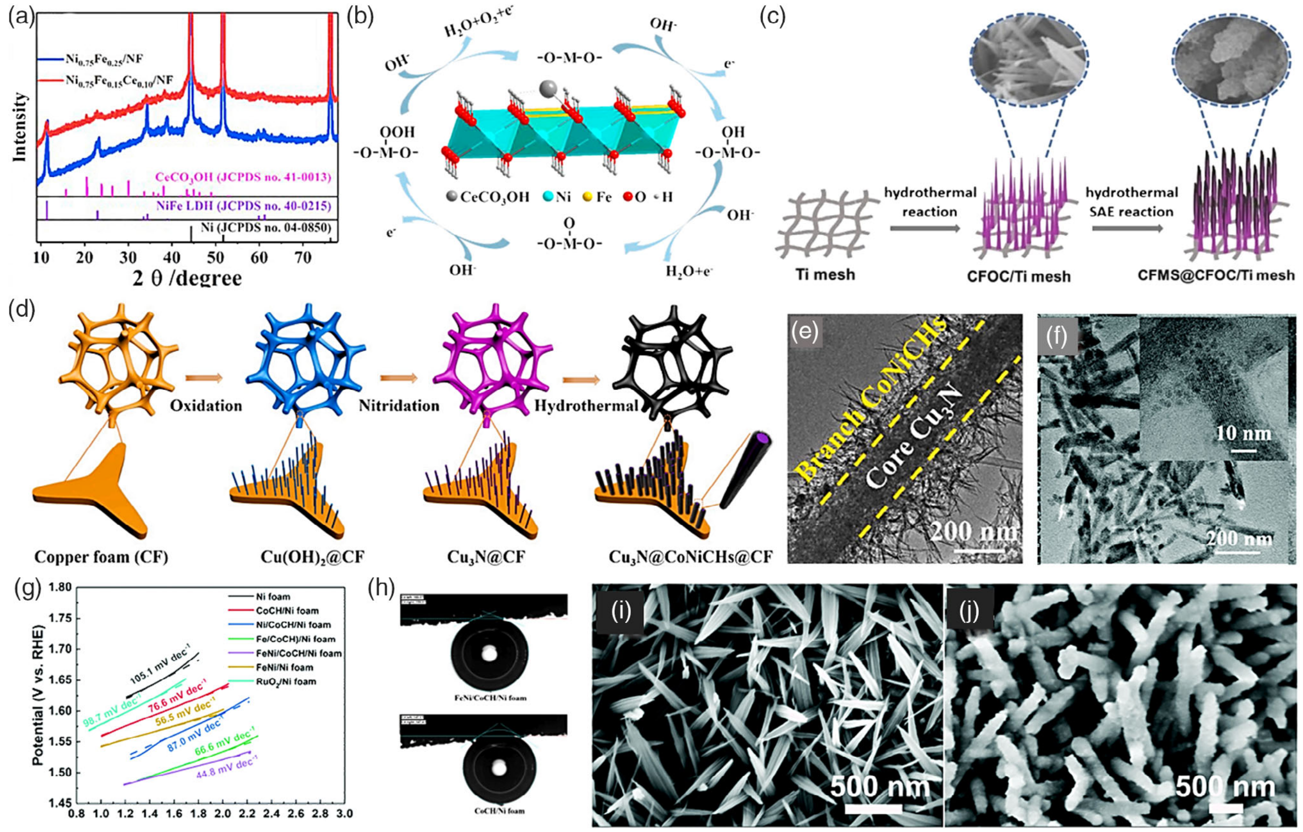

Figure 10. a). XRD patterns of the NiFe-LDH ($Ni_{0.75}Fe_{0.25}$/NF) and the hybrid with $CeCO_3OH$ ($Ni_{0.75}Fe_{0.15}Ce_{0.10}$/NF). b) Probable mechanistic pathway of OER using $CeCO_3OH$/NiFe LDH hybrid. Reproduced with permission.[94] Copyright 2020, Elsevier. c) Synthetic scheme of CFOC/Ti mesh and CFMS@CFOC/Ti mesh. Reproduced with permission.[95] Copyright 2020, Wiley-VCH GmbH. d) Schematic illustration of the formation of Cu_3N@CoNiCHs@CF and e) TEM image of Cu_3N@CoNiCHs showing the core–shell structure. Reproduced with permission.[96] Copyright 2021, Elsevier. f) TEM image of FeNi-QDs decorated CoCH/Ni foam (FeNi/CoCH/NF), g) Tafel plot for OER in 1.0 M KOH, and h) contact angle measurements of FeNi/CoCH/Ni foam and CoCH/Ni foam. Reproduced with permission.[97] Copyright 2022, The Royal Society of Chemistry. SEM images of: (i) CoCuCH/NF and j) NiOOH@CoCuCH nanorods. Reproduced with permission.[98] Copyright 2022, The Royal Society of Chemistry.

composed of amorphous cobalt–iron tetrathiomolybdate shell on crystalline Ti mesh-supported cobalt–iron carbonate hydroxide hydrate nanowire arrays (CFMS@CFOC/Ti mesh), as shown in Figure 10c. The hypothesis was that such an amorphous–crystalline combination would accelerate the charge transfer by increasing exposure of the active sites to the electrolyte and also improve the long-term structural stability of the electrode material. The high OER performance of CFMS@CFOC/Ti mesh was evidenced by the low overpotential (237 mV) requirement to deliver 10 mA cm^{-2} current density and good stability for 25 h in 1.0 M KOH.

To harness the interfacial interaction, Liu et al.[96] prepared a 3D hierarchical heterostructure of Cu_3N/Cu foam core and Co-Ni carbonate hydroxide (CoNiCH) shell (Figure 10d,e). The strong electronic interaction between Cu_3N and CoNiCH favored the OH^- adsorption on the electron-deficient CoNiCHs and fast electron transport in Cu_3N@CoNiCHs@CF. The controlled electrocatalytic investigations confirmed the more significant role of the compact heterointerface in this hybrid compared to that of the singular counterparts and physical mixtures of both components. The surprisingly high ECSA value of Cu_3N@CoNiCHs@CF indicated the availability of numerous electrochemically active OER sites, and its superhydrophilicity benefitted wettability, thereby increasing the electrolyte exposure. As a result of all these contributing factors, Cu_3N@CoNiCHs@CF demonstrated excellent OER performance ($\eta_{10} \approx 155$ mV) in 1.0 M KOH. In a recent study, Zhao et al.[97] employed FeNi-QD-decorated CoCH@Ni foam nanosword arrays (Figure 10f) as an efficient OER electrocatalyst in 1.0 M KOH. The FeNi/CoCH/Ni foam exhibited a low overpotential of $\approx$240 mV@20 mA cm^{-2} and a Tafel slope (Figure 10g) of $\approx$44.8 mV dec^{-1} for OER. Such an efficient oxygen evolution activity was attributed to the synergistic interaction of FeNi-alloy QDs with CoCH, which modified the electronic structure of the electrocatalyst surface and also improved the mass transfer by facilitating a rapid bubble release due to the low interfacial adhesion, consequently accelerating the reaction kinetics (Figure 10h). It was also identified that Fe played a key role in tailoring the OER performance of CoCH. Another recent report presented the efficient alkaline OER activity of a hybrid obtained by electrodepositing NiOOH on Ni-foam-supported CuCo carbonate hydroxide nanorods

(NiOOH@CoCuCH@NF), as shown in Figure 10i,j.[98] This hybrid exhibited a lower OER overpotential ($\eta_{10} \approx 263$ mV) than its individual components in 1.0 M KOH. The enhanced OER performance of NiOOH@CoCuCH@NF could be attributed to the availability of numerous active sites, firm NiOOH–CuCoCH interface enabled rapid charge transfer, and quick release of gas bubbles facilitating the mass transport. In addition, the strong adhesion of NiOOH@CoCuCH to the Ni foam improved the stability of the electrode for long-term electrolysis.

7. Conclusions and Prospects

Easily synthesizable layered metal carbonate hydroxides have been less explored for electrocatalytic water splitting instead of their considerable hydrophilicity. However, recently, this class of materials has gained attention as active electrode materials for water electrolysis. The main challenges associated with monometallic TMCHs as alkaline OER electrocatalysts are their low electrical conductivity, limited number of available active sites, low intrinsic activity, and poor durability due to metal dissolution during long-term usage.[58] In this regard, multimetallic carbonate hydroxides have attracted considerable interest over the past few years. The present review summarizes various modulation strategies—compositional tuning, heteroatom doping/substitution, morphology engineering, in situ electrochemical transformation, and hybrid/heterostructure fabrication. A comprehensive discussion of these strategies would be beneficial for the design and fabrication of highly efficient OER electrocatalysts in alkaline media. Briefly, achieving an optimized MTMCH composition in terms of high OER performance via compositional tuning could pave the way for the fabrication of prospective OER electrocatalysts with more active sites than their monometallic counterparts. Doping/substitution is highly advantageous for modifying the electronic structure to regulate the d-band electron density, improve the electrical conductivity, and lower the activation energy barrier of the rate-limiting step. In addition, morphology engineering and in situ electrochemical transformations, including phase transition, enhance the OER by enhancing the ECSA of the electrode materials via better electrolyte exposure and in situ generation of highly reactive chemical species that serve as the real active sites. Another effective approach is the fabrication of a hybrid/heterostructure, in which the synergistic interaction between the individual components in the hybrid plays a crucial role in boosting the OER activity. Despite the exploration of various effective strategies, there is still much room left for the advancement of MTMCHs as highly efficient electrocatalysts for water electrolysis.

In this regard, the following points can be regarded as future perspectives for the application of MTMCHs as superefficient water-splitting electrocatalysts. First, the crystal structure of MTMCHs is still debated, so the structure–activity relationship should be investigated further to better the understanding. Second, the precise and accurate identification of the true active sites in MTMCH-based OER electrocatalysts by ex situ characterization is still challenging. Thus, in situ or operando spectroscopic and microscopic techniques should be adopted to determine the real OER active species. In addition, theoretical insights would also enhance the understanding of the mechanistic pathways of the alkaline OER in MTMCHs. Third, MTMCHs are likely to undergo surface reconstruction or phase transition during the alkaline OER along with metal dissolution, which is associated with serious performance degradation. In practice, electrode materials that can deliver $\approx$1 A cm^{-2} current density for more than 1000 h are desirable for industrial applications.[152] To improve the long-term stability, structural integrity, and also electronic conductivity of the electrode materials, the strategy of introducing protective layers of carbonaceous components can be adopted.

In conclusion, mixed transition metal carbonate hydroxide-based materials with the available reported strategies can be beneficial for the development of promising OER electrocatalysts. Furthermore, highly efficient alkaline oxygen-evolving electrocatalysts can be suitably designed and fabricated by combining advanced operando techniques and theoretical determination of the precise structure–activity relationships to satisfy the rising demand for large-scale industrial applications in favor of the hydrogen-fuel economies.

Acknowledgements

A.K. and H.S.C. contributed equally to this work. This work was supported by the National Research Foundation of Korea (NRF) grant funded by the Korean Government (MSIT) (Nos. 2019R1A2C1086075 and 2021R1A4A2001687).

Conflict of Interest

The authors declare no conflict of interest.

Keywords

alkaline medium, electrocatalysts, metal carbonate hydroxides, mixed metals, oxygen evolution reactions

Received: May 6, 2022
Revised: May 26, 2022

[1] N. S. Lewis, D. G. Nocera, *Proc. Natl. Acad. Sci. U.S.A.* **2006**, *103*, 15729.
[2] A. J. Bard, M. A. Fox, *Acc. Chem. Res.* **1995**, *28*, 141.
[3] F. Ferrara, in *Industrial Engineering*, University of Cagliari, Cagliari, Italy **2007**.
[4] M. S. Burke, L. J. Enman, A. S. Batchellor, S. Zou, S. W. Boettcher, *Chem. Mater.* **2015**, *27*, 7549.
[5] X. F. Lu, G. R. Li, Y. X. Tong, *Sci. China Technol. Sci.* **2015**, *58*, 1799.
[6] A. Li, Y. Sun, T. Yao, H. Han, *Chem. Eur. J.* **2018**, *24*, 18334.
[7] J. A. Turner, *Science* **2004**, *305*, 972.
[8] M. Conte, F. di Mario, A. Iacobazzi, A. Mattucci, A. Moreno, M. Ronchetti, *Energies* **2009**, *2*, 150.
[9] P. E. Dodds, S. Demoullin, *Int. J. Hydrogen Energy* **2013**, *38*, 7189.
[10] T. A. Napp, A. Gambhir, T. P. Hills, N. Florin, P. S. Fennell, *Renew. Sustain. Energy Rev.* **2014**, *30*, 616.
[11] G. W. Crabtree, M. S. Dresselhaus, M. V. Buchanan, *Phys. Today* **2004**, *57*, 39.
[12] J. D. Holladay, J. Hu, D. L. King, Y. Wang, *Catal. Today* **2009**, *139*, 244.
[13] M. Balat, *Int. J. Hydrogen Energy* **2008**, *33*, 4013.

[14] P. A. Pilavachi, A. I. Chatzipanagi, A. I. Spyropoulou, *Int. J. Hydrogen Energy* **2009**, *34*, 5294.
[15] J. R. Rostrup-Nielsen, T. Rostrup-Nielsen, *Cattech* **2002**, *6*, 150.
[16] K. Christopher, R. Dimitrios, *Energy Environ. Sci.* **2012**, *5*, 6640.
[17] C. Tang, L. Gan, R. Zhang, W. Lu, X. Jiang, A. M. Asiri, X. Sun, J. Wang, L. Chen, *Nano Lett.* **2016**, *16*, 6617.
[18] O. Schmidt, A. Gambhir, I. Staffell, A. Hawkes, J. Nelson, S. Few, *Int. J. Hydrogen Energy* **2017**, *42*, 30470.
[19] Y. Liu, L. J. Cao, C. W. Cao, M. Wang, K. L. Leung, S. S. Zeng, T. F. Hung, C. Y. Chung, Z. G. Lu, *Chem. Commun.* **2014**, *50*, 14635.
[20] C. Hu, L. Zhang, J. Gong, *Energy Environ. Sci.* **2019**, *12*, 2620.
[21] J. Lee, B. Jeong, J. D. Ocon, *Curr. Appl. Phys.* **2013**, *13*, 309.
[22] A. Karmakar, S. K. Srivastava, *J. Mater. Chem. A* **2019**, *7*, 15054.
[23] A. Karmakar, S. K. Srivastava, *ACS Appl. Mater. Interfaces* **2017**, *9*, 22378.
[24] Q. Pan, L. Wang, *J. Power Sources* **2021**, *485*, 229335.
[25] C. Zhu, D. Wen, S. Leubner, M. Oschatz, W. Liu, M. Holzschuh, F. Simon, S. Kaskel, A. Eychmüller, *Chem. Commun.* **2015**, *51*, 7851.
[26] H. Wang, H. W. Lee, Y. Deng, Z. Lu, P. C. Hsu, Y. Liu, D. Lin, Y. Cui, *Nat. Commun.* **2015**, *6*, 1.
[27] Y. Sun, S. Gao, F. Lei, J. Liu, L. Liang, Y. Xie, *Chem. Sci.* **2014**, *5*, 3976.
[28] H. Wu, T. Yang, Y. Du, L. Shen, G. Wei Ho, H. Wu, G. W. Ho, T. Yang, L. Shen, Y. Du, *Adv. Mater.* **2018**, *30*, 1804341.
[29] J. G. Lee, J. Hwang, H. J. Hwang, O. S. Jeon, J. Jang, O. Kwon, Y. Lee, B. Han, Y. G. Shul, *J. Am. Chem. Soc.* **2016**, *138*, 3541.
[30] B. Weng, F. Xu, C. Wang, W. Meng, C. R. Grice, Y. Yan, *Energy Environ. Sci.* **2017**, *10*, 121.
[31] N. Li, D. K. Bediako, R. G. Hadt, D. Hayes, T. J. Kempa, F. von Cube, D. C. Bell, L. X. Chen, D. G. Nocera, *Proc. Natl. Acad. Sci. U. S. A.* **2017**, *114*, 1486.
[32] X. Li, J. Wei, Q. Li, S. Zheng, Y. Xu, P. Du, C. Chen, J. Zhao, H. Xue, Q. Xu, H. Pang, X. R. Li, J. L. Wei, Q. Li, S. S. Zheng, Y. X. Xu, H. G. Xue, Q. Xu, H. Pang, P. Du, C. Y. Chen, J. Y. Zhao, *Adv. Funct. Mater.* **2018**, *28*, 1800886.
[33] Q. Liu, H. Wang, X. Wang, R. Tong, X. Zhou, X. Peng, H. Wang, H. Tao, Z. Zhang, *Int. J. Hydrog. Energy* **2017**, *42*, 5560.
[34] H. S. Jadhav, A. Roy, B. Z. Desalegan, J. G. Seo, *Sustain. Energy Fuels* **2019**, *4*, 312.
[35] J. X. Feng, S. H. Ye, H. Xu, Y. X. Tong, G. R. Li, J. X. Feng, S. H. Ye, H. Xu, Y. X. Tong, G. R. Li, *Adv. Mater.* **2016**, *28*, 4698.
[36] H. Li, Q. Zhou, F. Liu, W. Zhang, Z. Tan, H. Zhou, Z. Huang, S. Jiao, Y. Kuang, *Appl. Catal. B Environ.* **2019**, *255*, 117755.
[37] C. Hu, L. Zhang, Z.-J. Zhao, J. Luo, J. Shi, Z. Huang, J. Gong, C. Hu, L. Zhang, Z. Zhao, Z. Huang, P. J. Gong, J. Luo, J. Shi, *Adv. Mater.* **2017**, *29*, 1701820.
[38] F. Song, X. Hu, *J. Am. Chem. Soc.* **2014**, *136*, 16481.
[39] A. Bergmann, E. Martinez-Moreno, D. Teschner, P. Chernev, M. Gliech, J. F. de Araújo, T. Reier, H. Dau, P. Strasser, *Nat. Commun.* **2015**, *6*, 1.
[40] D. Chen, M. Qiao, Y. R. Lu, L. Hao, D. Liu, C. L. Dong, Y. Li, S. Wang, *Angew. Chem. Int. Ed.* **2018**, *57*, 8691.
[41] R. Zhang, Y. C. Zhang, L. Pan, G. Q. Shen, N. Mahmood, Y. H. Ma, Y. Shi, W. Jia, L. Wang, X. Zhang, W. Xu, J. J. Zou, *ACS Catal.* **2018**, *8*, 3803.
[42] W. Chen, H. Wang, Y. Li, Y. Liu, J. Sun, S. Lee, J. S. Lee, Y. Cui, *ACS Cent. Sci.* **2015**, *1*, 244.
[43] Y. Wang, Y. Zhu, S. Zhao, S. She, F. Zhang, Y. Chen, T. Williams, T. Gengenbach, L. Zu, H. Mao, W. Zhou, Z. Shao, H. Wang, J. Tang, D. Zhao, C. Selomulya, *Matter* **2020**, *3*, 2124.
[44] Y. Zhang, H. Guo, P. Yuan, K. Pang, B. Cao, X. Wu, L. Zheng, R. Song, *J. Power Sources* **2019**, *442*, 227252.
[45] F. Wu, Z. Yao, K. Huang, B. Zhang, J. Xia, Z. Chen, J. Wu, *J. Mater. Res. Technol.* **2021**, *15*, 6721.
[46] C. Maccato, L. Bigiani, L. Girardi, A. Gasparotto, O. I. Lebedev, E. Modin, D. Barreca, G. A. Rizzi, *Adv. Mater. Interfaces* **2021**, *8*, 2100763.
[47] Z. Y. Yu, Y. Duan, J. D. Liu, Y. Chen, X. K. Liu, W. Liu, T. Ma, Y. Li, X. S. Zheng, T. Yao, M. R. Gao, J. F. Zhu, B. J. Ye, S. H. Yu, *Nat. Commun.* **2019**, *10*, 2799.
[48] J. Yin, Y. Li, F. Lv, M. Lu, K. Sun, W. Wang, L. Wang, F. Cheng, Y. Li, P. Xi, S. Guo, *Adv. Mater.* **2017**, *29*, 1704681.
[49] P. Xi, B. Huang, J. Yin, J. Jin, M. Lu, H. Zhang, Y. Peng, C. H. Yan, *J. Am. Chem. Soc.* **2020**, *142*, 18378.
[50] J. Yin, J. Jin, H. Zhang, M. Lu, Y. Peng, B. Huang, P. Xi, C. Yan, *Angew. Chem. Int. Ed.* **2019**, *131*, 18849.
[51] W. Shen, J. Jin, Y. Hu, Y. Hou, J. Yin, Z. Ma, Y.-Q. Zhao, P. Xi, *Chinese J. Catal.* **2022**, *43*, 1485.
[52] N. T. Suen, S. F. Hung, Q. Quan, N. Zhang, Y. J. Xu, H. M. Chen, *Chem. Soc. Rev.* **2017**, *46*, 337.
[53] Z. Chen, X. Duan, W. Wei, S. Wang, B. J. Ni, *J. Mater. Chem. A* **2019**, *7*, 14971.
[54] S. Liu, K. S. Hui, K. N. Hui, V. V. Jadhav, Q. X. Xia, J. M. Yun, Y. R. Cho, R. S. Mane, K. H. Kim, *Electrochim. Acta* **2016**, *188*, 898.
[55] L. Hui, Y. Xue, D. Jia, H. Yu, C. Zhang, Y. Li, *Adv. Energy Mater.* **2018**, *8*, 1800175.
[56] T. Tang, W. J. Jiang, S. Niu, L. P. Yuan, J. S. Hu, L. J. Wan, *J. Mater. Chem. A* **2019**, *7*, 21959.
[57] M. Cai, X. Lu, Z. Zou, K. Guo, P. Xi, C. Xu, *ACS Sustain. Chem. Eng.* **2019**, *7*, 6161.
[58] X. Zhang, H. Yi, Q. An, S. Song, *J. Alloys Compd.* **2021**, *887*, 161405.
[59] W. Wang, M. Kong, Y. Yao, N. Wei, M. Ma, *Micro Nano Lett.* **2017**, *12*, 264.
[60] K. Sun, X. Zhang, X. Guo, X. Zhai, Y. M. Yan, Q. Xiao, Y. Xue, L. Jing, Y. Zhang, *J. Power Sources* **2015**, *278*, 464.
[61] K. L. Zhou, C. Wang, Z. Wang, C. B. Han, Q. Zhang, X. Ke, J. Liu, H. Wang, *Energy Environ. Sci.* **2020**, *13*, 3082.
[62] X. Li, X. Hao, A. Abudula, G. Guan, *J. Mater. Chem. A* **2016**, *4*, 11973.
[63] C. Yuan, H. B. Wu, Y. Xie, X. W. Lou, *Angew. Chem., Int. Ed.* **2014**, *53*, 1488.
[64] F. Wu, J. Bai, J. Feng, S. Xiong, *Nanoscale* **2015**, *7*, 17211.
[65] L. Hu, L. Wu, M. Liao, X. Hu, X. Fang, *Adv. Funct. Mater.* **2012**, *22*, 998.
[66] T. Y. Wei, C. H. Chen, H. C. Chien, S. Y. Lu, C. C. Hu, *Adv. Mater.* **2010**, *22*, 347.
[67] Y. Wang, W. Ding, S. Chen, Y. Nie, K. Xiong, Z. Wei, *Chem. Commun.* **2014**, *50*, 15529.
[68] J. Li, X. Li, Y. Luo, Q. Cen, Q. Ye, X. Xu, F. Wang, *Int. J. Hydrogen Energy* **2018**, *43*, 9635.
[69] Y. Jia, Y. N. Li, Z. M. Wang, F. M. Li, P. J. Jin, S. N. Li, Y. Chen, *Chem. Eng. J.* **2021**, *417*, 128066.
[70] Y. Yan, *Front. Chem.* **2021**, *9*, 754357.
[71] G. Li, F. Li, Y. Zhao, W. Li, Z. Zhao, Y. Li, H. Yang, K. Fan, P. Zhang, L. Sun, *ACS Sustain. Chem. Eng.* **2021**, *9*, 905.
[72] K. Karthick, S. Anantharaj, S. R. Ede, S. Kundu, *Inorg. Chem.* **2019**, *58*, 1895.
[73] K. Karthick, S. Subhashini, R. Kumar, S. Sethuram Markandaraj, M. M. Teepikha, S. Kundu, *Inorg. Chem.* **2020**, *59*, 16690.
[74] Y. Yang, X. Luan, X. Dai, X. Zhang, H. Qiao, H. Zhao, J. Yong, L. Yu, J. Han, J. Zhang, *Electrochim. Acta* **2019**, *309*, 57.
[75] T. Tang, W. J. Jiang, S. Niu, N. Liu, H. Luo, Y. Y. Chen, S. F. Jin, F. Gao, L. J. Wan, J. S. Hu, *J. Am. Chem. Soc.* **2017**, *139*, 8320.
[76] A. Karmakar, S. K. Srivastava, *ACS Appl. Energy Mater.* **2020**, *3*, 7335.
[77] Y. F. Qi, Q. Wang, X. G. Wang, Z. Y. Liu, X. J. Zhao, E. C. Yang, *Nanoscale* **2019**, *11*, 10595.
[78] W. Zhu, G. Zhu, J. Hu, Y. Zhu, H. Chen, C. Yao, Z. Pi, S. Zhu, E. Li, *Inorg. Chem. Commun.* **2020**, *114*, 107851.

[79] M. Jin, J. Li, J. Gao, W. Liu, J. Han, H. Liu, D. Zhan, L. Lai, *J. Colloid Interface Sci.* **2021**, *587*, 581.
[80] J. Zhao, X. Liu, X. Ren, B. Du, X. Kuang, D. Tian, Q. Wei, D. Wu, *J. Colloid Interface Sci.* **2022**, *609*, 414.
[81] M. Dai, H. Fan, G. Xu, M. Wang, S. Zhang, L. Lu, Y. Zhang, *J. Power Sources* **2020**, *450*, 227639.
[82] P. Wang, L. Zhang, Z. Wang, D. Bu, K. Zhan, Y. Yan, J. Yang, B. Zhao, *J. Colloid Interface Sci.* **2021**, *597*, 361.
[83] S. Zhang, B. Ni, H. Li, H. Lin, H. Zhu, H. Wang, X. Wang, *Chem. Commun.* **2017**, *53*, 8010.
[84] H. Sun, Y. Miao, T. Wu, Q. Wang, *Chem. Commun.* **2020**, *56*, 872.
[85] S. Zhang, B. Huang, L. Wang, X. Zhang, H. Zhu, X. Zhu, J. Li, S. Guo, E. Wang, *ACS Appl. Mater. Interfaces* **2020**, *12*, 40220.
[86] J. Liu, H. Li, J. Cai, J. Liu, Y. Liu, Z. Sun, X. He, D. Qu, X. Li, *Inorg. Chem. Front.* **2022**, *9*, 1819.
[87] L. Xie, C. Tang, K. Wang, G. Du, A. M. Asiri, X. Sun, *Small* **2017**, *13*, 1602755.
[88] J. Kang, J. Sheng, J. Xie, H. Ye, J. Chen, X. Z. Fu, G. Du, R. Sun, C. P. Wong, *J. Mater. Chem. A* **2018**, *6*, 10064.
[89] A. Indra, U. Paik, T. Song, *Angew. Chem. Int. Ed.* **2018**, *57*, 1241.
[90] J. Chi, H. Yu, G. Jiang, J. Jia, B. Qin, B. Yi, Z. Shao, *J. Mater. Chem. A* **2018**, *6*, 3397.
[91] F. Wang, K. Ma, W. Tian, J. Dong, H. Han, H. Wang, K. Deng, H. Yue, Y. X. Zhang, W. Jiang, J. Ji, *J. Mater. Chem. A* **2019**, *7*, 19589.
[92] J. Kang, J. Chen, J. Sheng, J. Xie, X. Z. Fu, R. Sun, C. P. Wong, *ACS Sustain. Chem. Eng.* **2019**, *7*, 16459.
[93] J. Cai, J. Huang, S. Xu, L. Yuan, X. Huang, Z. Huang, C. Zhang, *J. Solid State Electrochem.* **2019**, *23*, 3449.
[94] J. Ding, Y. Han, G. Hong, *Int. J. Hydrogen Energy* **2021**, *46*, 2018.
[95] J. Zhao, X. Ren, X. Sun, Y. Zhang, T. Yan, Q. Wei, D. Wu, *ChemElectroChem* **2020**, *7*, 2309.
[96] S. Q. Liu, M. R. Gao, S. Liu, J. L. Luo, *Appl. Catal. B: Environ.* **2021**, *292*, 120148.
[97] M. Zhao, J. Du, H. Lei, L. Pei, Z. Gong, X. Wang, H. Bao, *Nanoscale* **2022**, *14*, 3191.
[98] B. Li, K. Wang, J. Ren, P. Qu, *New J. Chem.* **2022**, *46*, 7615.
[99] J. Du, S. Xu, L. Sun, F. Li, *Chem. Commun.* **2019**, *55*, 14773.
[100] S. Anantharaj, S. R. Ede, K. Sakthikumar, K. Karthick, S. Mishra, S. Kundu, *ACS Catal.* **2016**, *6*, 8069.
[101] B. S. Yeo, A. T. Bell, *J. Am Chem. Soc.* **2011**, *133*, 5587.
[102] S. Marini, P. Salvi, P. Nelli, R. Pesenti, M. Villa, M. Berrettoni, G. Zangari, Y. Kiros, *Electrochim. Acta* **2012**, *82*, 384.
[103] F. Song, L. Bai, A. Moysiadou, S. Lee, C. Hu, L. Liardet, X. Hu, *J. Am. Chem. Soc.* **2018**, *140*, 7748.
[104] Z. Ma, Y. Zhang, S. Liu, W. Xu, L. Wu, Y. C. Hsieh, P. Liu, Y. Zhu, K. Sasaki, J. N. Renner, K. E. Ayers, R. R. Adzic, J. X. Wang, *J. Electro. Chem.* **2018**, *819*, 296.
[105] J. Rossmeisl, A. Logadottir, J. K. Nørskov, *Chem. Phys.* **2005**, *319*, 178.
[106] J. Rossmeisl, Z. W. Qu, H. Zhu, G. J. Kroes, J. K. Nørskov, *J. Electro. Chem.* **2007**, *607*, 83.
[107] G. Mattioli, P. Giannozzi, A. Amore Bonapasta, L. Guidoni, *J. Am. Chem. Soc.* **2013**, *135*, 15353.
[108] H. Dau, C. Limberg, T. Reier, M. Risch, S. Roggan, P. Strasser, *ChemCatChem* **2010**, *2*, 724.
[109] A. Valdés, J. Brillet, M. Grätzel, H. Gudmundsdóttir, H. A. Hansen, H. Jónsson, P. Klüpfel, G. J. Kroes, F. Le Formal, I. C. Man, R. S. Martins, J. K. Nørskov, J. Rossmeisl, K. Sivula, A. Vojvodic, M. Zäch, *Phy. Chem. Chem. Phy.* **2012**, *14*, 49.
[110] A. V. Akimov, J. T. Muckerman, O. V. Prezhdo, *J. Am. Chem. Soc.* **2013**, *135*, 8682.
[111] A. J. Bard, L. R. Faulkner, in *Electrochemical Methods: Fundamentals And Applications*, Wiley & Sons, Inc., Hoboken **2001**.
[112] I. R. Barba, *Ph.D. Thesis, University of Glasgow* **2017**.
[113] S. Anantharaj, S. R. Ede, K. Karthick, S. Sam Sankar, K. Sangeetha, P. E. Karthik, S. Kundu, *Energy Environ. Sci.* **2018**, *11*, 744.
[114] Y. Xu, K. Fan, Y. Zou, H. Fu, M. Dong, Y. Dou, Y. Wang, S. Chen, H. Yin, M. Al-Mamun, P. Liu, H. Zhao, *Nanoscale* **2021**, *13*, 20324.
[115] W. Shen, J. Yin, J. Jin, Y. Hu, Y. Hou, J. Xiao, Y. Q. Zhao, P. Xi, *Adv. Energy Sustain. Res.* **2022**, 2200036.
[116] Y. H. Wang, M. M. Liang, Y. J. Zhang, S. Chen, P. Radjenovic, H. Zhang, Z. L. Yang, X. S. Zhou, Z. Q. Tian, J. F. Li, *Angew. Chem. Int. Ed.* **2018**, *57*, 11257.
[117] G. Kang, M. Yang, M. S. Mattei, G. C. Schatz, R. P. van Duyne, *Nano Lett.* **2019**, *19*, 2106.
[118] Z. Qiu, C. W. Tai, G. A. Niklasson, T. Edvinsson, *Energy Environ. Sci.* **2019**, *12*, 572.
[119] H. Ali-Löytty, M. W. Louie, M. R. Singh, L. Li, H. G. Sanchez Casalongue, H. Ogasawara, E. J. Crumlin, Z. Liu, A. T. Bell, A. Nilsson, D. Friebel, *J. Phys. Chem. C* **2016**, *120*, 2247.
[120] D. Friebel, M. W. Louie, M. Bajdich, K. E. Sanwald, Y. Cai, A. M. Wise, M. J. Cheng, D. Sokaras, T. C. Weng, R. Alonso-Mori, R. C. Davis, J. R. Bargar, J. K. Nørskov, A. Nilsson, A. T. Bell, *J. Am. Chem. Soc.* **2015**, *137*, 1305.
[121] L. Trotochaud, J. K. Ranney, K. N. Williams, S. W. Boettcher, *J. Am. Chem. Soc.* **2012**, *134*, 17253.
[122] Y. Yan, B. Y. Xia, B. Zhao, X. Wang, *J. Mater. Chem. A* **2016**, *4*, 17587.
[123] K. L. Pickrahn, S. W. Park, Y. Gorlin, H. B. R. Lee, T. F. Jaramillo, S. F. Bent, *Adv. Energy Mater.* **2012**, *2*, 1269.
[124] S. Anantharaj, K. Karthick, S. Kundu, *Mater. Today Energy* **2017**, *6*, 1.
[125] N. Asim, S. Ahmadi, M. A. Alghoul, F. Y. Hammadi, K. Saeedfar, K. Sopian, *Int. J. Photoenergy* **2014**, *2014*, 1.
[126] X. Li, P. F. Liu, L. Zhang, M. Y. Zu, Y. X. Yang, H. G. Yang, *Chem. Commun.* **2016**, *52*, 10566.
[127] S. Anantharaj, S. Noda, *Small* **2020**, *16*, 1905779.
[128] C. G. Morales-Guio, L. Liardet, X. Hu, *J. Am. Chem. Soc.* **2016**, *138*, 8946.
[129] M. W. Kanan, Y. Surendranath, D. G. Nocera, *Chem. Soc. Rev.* **2009**, *38*, 109.
[130] Z. Yan, H. Liu, Z. Hao, M. Yu, X. Chen, J. Chen, *Chem. Sci.* **2020**, *11*, 10614.
[131] P. E. Lokhande, U. S. Chavan, A. Pandey, *Electrochem. Energy Rev.* 2020, *3*, 155.
[132] S. Wang, G. Lü, W. Tang, *Powder Diffr.* **2010**, *25*, S7.
[133] J. Yang, H. Cheng, R. L. Frost, *Spectrochim. Acta A.* **2011**, *78*, 420.
[134] B. Li, Y. Xie, C. Wu, Z. Li, J. Zhang, *Mater. Chem. Phy.* **2006**, *99*, 479.
[135] P. Bhojane, A. le Bail, P. M. Shirage, *Acta Cryst.* **2019**, *75*, 61.
[136] A. Grimaud, K. J. May, C. E. Carlton, Y.-L. Lee, M. Risch, W. T. Hong, J. Zhou, Y. Shao-Horn, *Nat. Commun.* **2013**, *4*, 2439.
[137] K. Fominykh, P. Chernev, I. Zaharieva, J. Sicklinger, G. Stefanic, M. Döblinger, A. Müller, A. Pokharel, S. Böcklein, C. Scheu, T. Bein, D. Fattakhova-Rohlfing, *ACS Nano* **2015**, *9*, 5180.
[138] X. Li, W. Xue, R. Mo, S. Yang, H. Li, J. Zhong, *Chinese J. Catal.* **2019**, *40*, 1576.
[139] H.-J. Lee, D.-H. Park, W.-J. Lee, S.-B. Han, M.-H. Kim, J.-H. Byeon, K.-W. Park, *Appl. Catal. A: Gen.* **2021**, *626*, 118377.
[140] Y. Gao, J. Bai, T. Zhou, Y. Gong, *Dalton Trans.* **2022**, *22*, 8832.
[141] L. A. Huang, H. Shin, W. A. Goddard, J. Wang, *Nano Energy* **2020**, *75*, 104885.
[142] R. Fan, Q. Mu, Z. Wei, Y. Peng, M. Shen, *J. Mater. Chem. A* **2020**, *8*, 9871.
[143] L. Tian, Z. Li, X. Xu, C. Zhang, *J. Mater. Chem. A* **2021**, *9*, 13459.
[144] S. Li, C. Xi, Y. Z. Jin, D. Wu, J. Q. Wang, T. Liu, H. B. Wang, C. K. Dong, H. Liu, S. A. Kulinich, X. W. Du, *ACS Energy Lett.* **2019**, *4*, 1823.

[145] K. Zhu, J. Chen, W. Wang, J. Liao, J. Dong, M. O. L. Chee, N. Wang, P. Dong, P. M. Ajayan, S. Gao, J. Shen, M. Ye, *Adv. Funct. Mater.* **2020**, *30*, 2003556.
[146] Z. Li, D. Liu, X. Lu, M. Du, Z. Chen, J. Teng, R. Sha, L. Tian, *Dalton Trans.* **2022**, *51*, 1527.
[147] J. X. Feng, H. Xu, Y. T. Dong, S. H. Ye, Y. X. Tong, G. R. Li, *Angew. Chem., Int. Ed.* **2016**, *55*, 3694.
[148] H. Sun, Z. Yan, F. Liu, W. Xu, F. Cheng, J. Chen, *Adv. Mater.* **2020**, *32*, 1806326.
[149] S. H. Bae, J. E. Kim, H. Randriamahazaka, S. Y. Moon, J. Y. Park, I. K. Oh, *Adv. Energy Mater.* **2017**, *7*, 1601492.
[150] B. Shang, P. Ma, J. Fan, L. Jiao, Z. Liu, Z. Zhang, N. Chen, Z. Cheng, X. Cui, W. Zheng, *Nanoscale* **2018**, *10*, 12330.
[151] X. Yan, L. Tian, S. Atkins, Y. Liu, J. Murowchick, X. Chen, *ACS Sustain. Chem. Eng.* **2016**, *4*, 3743.
[152] Y. Pan, X. Xu, Y. Zhong, L. Ge, Y. Chen, J. P. M. Veder, D. Guan, R. O'Hayre, M. Li, G. Wang, H. Wang, W. Zhou, Z. Shao, *Nat. Commun.* **2020**, *11*, 1.

Ayon Karmakar is a postdoctoral researcher at Chungbuk National University, South Korea with Prof. Sang Mun Jeong. Prior to the current position, Dr. Karmakar worked as a Postdoctoral Research Associate at Research Institute for Sustainable Energy, TCG-CREST, India and received his Ph.D. degree from the Indian Institute of Technology Kharagpur, India in 2020. His current research focus includes the development of non-precious electrode materials for energy conversion and storage applications.

Harish S. Chavan received his Ph.D. degree from Dongguk University in 2021. Currently, he is working as a postdoctoral researcher at Chungbuk National University under the guidance of Prof. Jung Sang Cho. His current research is focused on the synthesis of nanocomposite materials as electrocatalysts for overall water splitting and energy storage applications.

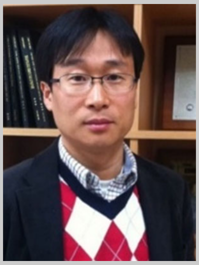

Sang Mun Jeong is a professor in the Department of Chemical Engineering, Chungbuk National University. He is a leader of Basic Research Laboratories (BRL) funded by the National Research Foundation (NRF) of South Korea. His research focuses on designing energy materials, understanding the electrode surface phenomena, developing eco-friendly electrochemical process, and energy storage devices.

Jung Sang Cho received his Ph.D. from the Interdisciplinary Program for Bioengineering, Seoul National University, Korea in 2013, and had post-doc experience at the Department of Materials Science and Engineering, Korea University, Korea (2014–2016). He has been a professor at the Department of Engineering Chemistry, Chungbuk National University, Cheongju, Korea, since 2016. His research group works on the development of nanostructured materials for energy storage, sensors, catalysts, displays, and biomaterials. For details, please visit the lab website: https://jjj777.wixsite.com/professor-cho.